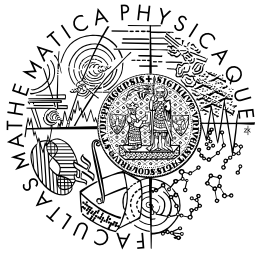

FACULTY
OF MATHEMATICS
AND PHYSICS
Charles University

MASTER THESIS

Šimon Midlik

Generation and detection of quantum turbulence in He II by second sound

Department of Low-Temperature Physics

Supervisor of the master thesis:	RNDr. David Schmoranzer, Ph.D.
Study programme:	Physics
Study branch:	Physics of condensed matter and materials

Prague 2019

I declare that I carried out this master thesis independently, and only with the cited sources, literature and other professional sources.

I understand that my work relates to the rights and obligations under the Act No. 121/2000 Sb., the Copyright Act, as amended, in particular the fact that the Charles University has the right to conclude a license agreement on the use of this work as a school work pursuant to Section 60 subsection 1 of the Copyright Act.

In ..... date ..... signature of the author

I would like to take this opportunity to thank my supervisor, David Schmoranzer who lead me from the beginning of my time in the Laboratory of Superfluidity up to now, for passing his theoretical and practical knowledge, which was essential for the creation of this thesis. Also, I would like to thank him for the great amount of time spent during his mentoring.

I would also like to thank the consultants of this thesis, Emil Varga and Martin James Jackson for their contributions preparing the experiment, operating the software and for help during the "endless" measurements.

My thanks also go to Ladislav Skrbek, as the head of the department for giving me the opportunity to perform the research presented here.

Finally, I would like to thank once more all those mentioned above for fruitful discussions, which were very helpful in completing this thesis.

Title: Generation and detection of quantum turbulence in He II by second sound

Author: Šimon Midlik

Department: Department of Low-Temperature Physics

Supervisor: RNDr. David Schmoranzer, Ph.D., Department of Low-Temperature Physics

Abstract: We have performed a study of quantum turbulence generated in oscillatory counterflow as a continuation of previous experiments on various channel flows of superfluid helium, in the form of coflow, thermal DC counterflow and pure superflow. We have investigated its development, steady state properties and temporal decay, as well as the effect of the resonant mode used to generate the turbulence at three different temperatures, 1.45 K, 1.65 K and 1.83 K. The attenuation of low amplitude second sound, orientated perpendicularly to the long axis of the resonator, was used to determine the amount of quantized vortices created. One of the main goals of this work was to characterize the critical parameters for the onset of instabilities in oscillatory counterflow and to determine their values. Decay measurements of the vortex line density allowed us to distinguish between Vinen-type and Kolmogorov-type decays of quantum turbulence.

Keywords: superfluid helium, oscillatory counterflow, quantum turbulence, second sound

Contents

Introduction

The liquefaction of Helium ^{4}He is generally regarded as the beginning of low temperature physics. ^{4}He was discovered in 1868 by the French astronomer Jules Janssen and Norman Lockyer from England independently observed a previously unknown spectral line in the sun's spectrum during a solar eclipse. In 1895, William Ramsay isolated helium on Earth for the first time from uranium oxide ore. Today, natural gas is the most common source of helium with it constituting around 7% of natural gas deposits. ^{4}He was first liquefied on July 10th 1908 by Heike Kamerlingh Onnes. It was the last of the gases to be liquefied, with the lowest boiling point at 4.2 K at normal pressure. It was quickly followed by the discovery of the superconductivity of mercury in 1911, for which Kamerlingh Onnes received the 1913 Nobel prize in Physics.

After further studies of liquid helium, many more interesting and unique properties have been discovered. Mainly, the absence of a triple point, which can be seen in the phase diagram shown in Figure 1 and the fact that helium remains liquid until the lowest temperatures, unless high pressure is applied. Furthermore, when cooling by lowering the saturated vapour pressure, a phase transition to a new liquid phase can be observed. The behaviour of helium in this state is truly extraordinary and will be discussed in more detail later. This so-called superfluid transition is a second order phase transition occurring at 2.17 K (the λ-point) and is also known as λ-transition. Its name is connected with the shape of the temperature dependence of the heat capacity across the transition, as shown at Figure 2. The normal liquid phase at temperatures above the λ-point behaves as a classical fluid and we denote it as He I. The other low temperature phase, is called the superfluid phase, historically known as He II. The line separating He I and He II in the phase diagram is commonly called the λ-line.

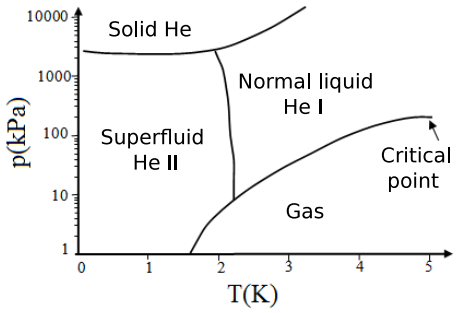

Figure 1: Phase diagram of ^{4}He.

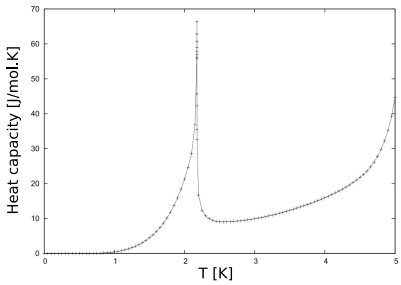

Figure 2: Temperature dependence of the heat capacity of ^{4}He around the superfluid transition.

The discovery of superfluidity in 1937 is generally attributed to Pyotr Kapitza, although Allen and Misener in Cambridge made the same discovery independently around the same time. For many years, a satisfactory theoretical description of superfluidity was missing. In the end, it was created by combining two different approaches. One was proposed by Lev Davidovich Landau, who correctly predicted the spectrum of thermal excitations in He II and the other by László

Tisza building on the theory of Bose-Einstein condensation. This led to the creation of the so-called two fluid model [1] which stated that the superfluid phase can be described as a mixture of two interpenetrating components: the normal component which behaves as a classical viscous fluid and carries all the entropy of the system and the superfluid component, which has zero viscosity and entropy. Unlike the normal component, the superfluid component can easily flow through various micro-porous materials [2] which may be used to design superleaks – components which act as solid obstacles for the normal component, but allow the superfluid through. Later experiments with torsionally oscillating discs in He II by Andronikashvili showed the temperature dependence of the density ratio of the two components, where the relative content of the superfluid component rises with decreasing temperature. This experiment hence proved the two fluid model, which leads to many interesting properties of He II.

The thermal conductivity of He II rises by six orders of magnitude during the transition, and is by far the highest of all known materials. Therefore during the transition, all boiling in the liquid stops, and only evaporation from the surface occurs. This leads to an atomically smooth surface. He II also creates a superfluid film that is up to 30 nm thick and wets almost all surfaces allowing it to flow out of any open container if its raised above the level of the ^{4}He bath. Another unique property of superfluid ^{4}He is the thermo-mechanical effect (or "fountain effect") where by creating a temperature gradient, a pressure gradient occurs as well. This effect is typically used for the creation of steady flows of superfluid helium generated by a fountain pump. By raising the temperature inside a cell closed by a superleak on one end and opened via a thin capillary on the other, pressure is increased as well, and a jet of superfluid helium appears above the capillary. The reverse effect also exists and is called the mechanocaloric effect.

It follows from the theory of Bose-Einstein condensation that any flow of the superfluid component should be strictly irrotational, which is not in agreement with experiments. It was Feynman who, at the suggestion of Onsager, theoretically explained this phenomenon. He showed that the superfluid may circulate only around so-called quantized vortices, and that the circulation can only have discrete values – multiples of the circulation quantum. Furthermore, it is energetically favorable to have multiple vortices each with a single quantum, rather than a single vortex with a higher circulation. Therefore, all of the vortices created in the superfluid component are the same (except for their length). We can describe a quantized vortex as the superfluid component circulating around an Angström-sized core. These vortices are topological defects, so they can only exist as closed loops or they have to start and end on a surface. If more vortices are created in the bulk, they may start to create a dense tangle and we can talk about quantum turbulence. In the low temperature limit, such a turbulent flow is a simpler counterpart [3] to classical turbulence. The best quantity for describing an amount of turbulence in the superfluid is the vortex line density, defining the length of all quantized vortices per unit volume. For temperatures over 1 K, the

[1] It is reasonable to consider this model only in the temperature range from λ-point to approximately 1 K. The content of the normal component below this temperature falls rapidly and becomes negligible below 0.7 K.

[2] For example sintered silver plugs or any small leaks.

[3] Mathematical model of such a flow is much simpler, so efficient numerical simulations are possible.

normal component must also be considered and the model of quantum turbulence becomes more complicated.

In He II, unique wave modes can be observed and explained by the two fluid model. Besides regular sound, called first sound here, where local variations in the total density appear, so-called second sound also exists in superfluid helium. In a second sound wave, the two components of He II move against each other resulting in local changes of the superfluid to normal component density ratio, which, from the two fluid model, is equivalent to local changes of temperature. Hence, we can consider second sound as waves of temperature. There are two more wave modes in He II: third sound, which appears on the thin film surface, and fourth sound which is observed in porous materials.

For a study of quantum turbulence, second sound is essential. As the normal component is strongly scattered on quantized vortices (due to mutual friction between the two components) the second sound wave is therefore attenuated if it propagates through a volume containing turbulence. By measuring the attenuation of the second sound amplitude, the vortex line density can be determined. This technique is commonly used for the detection of quantum turbulence in He II. The advantage of this technique is its simplicity, where only two moveable superleaks are needed. One is driven and operates as a generator of second sound and from the other the signal is read. When second sound is driven strongly enough, it should generate quantum turbulence on its own, in a similar fashion to steady counterflow, where the normal and superfluid components flow against each other.

One of the goals in recent studies is to observe and characterize the steady state properties of quantum turbulence and its temporal decay in various flows [4]. The most pressing problem is to distinguish between two different types of quantum turbulence: the Kolmogorov type, where on large scales the superfluid component imitates classical turbulent flows, and the Vinen type, which consists as a random tangle of quantized vortices. If He II flow is generated by a standing wave of the second sound, oscillating counterflow is present in anti-nodes of a resonant standing wave. Hence, the properties of quantum turbulence created by temperature waves may show unique behaviour in comparison to other generation techniques and warrant thorough investigation.

[4]Such flows are typically grid turbulence, oscillating mechanical flows around different resonators, thermally generated counterflow, the coflow of the both components and pure superflow.

1. Theoretical background

1.1 Classical fluid dynamics

1.1.1 Ideal fluids

To describe the macroscopic behaviour of a fluid, continuum theory is sufficient where spatial maps [1] of only five independent variables are required for the full determination of a system. First, we have to define a fluid particle, which is taken as macroscopic volume big enough to carry a large amount of atoms (molecules), yet small enough to move jointly and to be considered as a point object compared to the scale of the studied flow. The state of the chosen fluid particle is characterized by its velocity vector $\mathbf{v} = \mathbf{v}(\mathbf{r},\mathrm{t})$ and two thermodynamic state variables commonly chosen as the pressure $\mathrm{p}(\mathbf{r},\mathrm{t})$ and the density $\rho(\mathbf{r},\mathrm{t})$.

It is reasonable, for our purposes, to expect the conservation of mass for a fluidic system, which can be described by the equation of continuity [1]:

$$\frac{\partial \rho}{\partial t} + \nabla \cdot (\rho \mathbf{v}) = 0. \tag{1.1}$$

Here, the first term is giving a temporal change of fluid mass in the desired volume, whilst the second term is characterizing the amount of the fluid's mass flowing through the borders of the volume [2]. Furthermore, this equation must hold for any chosen volume of a fluid. The product under the divergence corresponds to the mass flux density $\mathbf{j} = \rho\mathbf{v}$, which is a vector with the same direction as the velocity and with an amplitude giving the fluid mass flowing per unit time per unit area perpendicular to the velocity.

The next step in the description of the considered system is to characterize its dynamics. Therefore, the derivation of the equation of motion for a fluid element is needed. In this work, we refer to Landau [1] and we show the equation of motion, generally known as Euler's equation, in the following form:

$$\frac{\partial \mathbf{v}}{\partial t} + (\mathbf{v} \cdot \nabla)\mathbf{v} = -\frac{1}{\rho}\nabla p. \tag{1.2}$$

It holds for the case of an ideal fluid and without the consideration of the effects of a gravitational field or any other external forces.

1.1.2 Viscous fluids

In the previous description, we did not consider the energy dissipation in the fluid's motion or the internal heat exchange between its parts. In real fluid motion, the dissipation of energy due to its viscosity - the internal friction between the fluid particles moving with different velocities - is always present. The equation of motion will therefore differ from that of an ideal fluid. The equation of

[1] We call this the Euler's approach of the continuum theory, where the individual particles are not tracked in time, but a time evolutionary map of variables is constructed on fixed mesh.

[2] The sign of the second term in the equation of continuity is characterizing a direction of mass flow. If the divergence term is positive here, then fluid mass is flowing out of the desired volume and vice versa

continuity 1.1 is still valid for viscous fluids. With the further assumption of the incompressibility of a fluid expressed as $\nabla \cdot \mathbf{v} = 0$, which is satisfied for most real fluids, the Euler's equation 1.2 takes the form of [1]:

$$\frac{\partial \mathbf{v}}{\partial t} + (\mathbf{v} \cdot \nabla)\mathbf{v} = -\frac{1}{\rho}\nabla p + \nu \triangle \mathbf{v}. \tag{1.3}$$

and is generally known as the Navier-Stokes equation. The new term on the right-hand side of the equation includes the kinematic viscosity ν which is a function of pressure and temperature and can also be given as the ratio of the dynamic viscosity η and fluid density. For steady flow, the velocity derivative with respect to time is identically equal to zero and equation 1.3 can be easily transformed into a dimensionless form by introducing the characteristic dimension L and velocity U of the studied flow. Through the characteristic quantities, we can define the dimensionless velocity $v' = v/U$, dimension $r' = r/L$ and pressure $p' = p/(\rho U^2)$. For a steady flow with the newly defined dimensionless quantities for the Navier-Stokes equation we get:

$$(\mathbf{v}' \cdot \nabla')\mathbf{v}' = -\nabla' p' + \frac{1}{Re}\triangle' \mathbf{v}'. \tag{1.4}$$

Here we have defined the Reynolds number, which is the only parameter needed for determination of the dynamical behaviour of geometrically similar flows. The Reynolds number is given as:

$$Re = \frac{UL}{\nu} \tag{1.5}$$

and denotes relative importance of viscous drag and inertial forces in the studied flow. For Re $\gg 1$, inertial forces dominate and instabilities may occur in the flow.

1.1.3 Turbulent flows

A rigorous definition of turbulence is yet still unknown, but we can describe its characteristic features. Turbulent flow is said to be random, chaotic, diffusive and consisting of non-trivial rotational flows with vortex structures on a wide range of scales. We can divide the velocity field of a turbulent flow into the mean flow velocity field and velocity fluctuations. This approach is called the Reynolds decomposition. The mean flow velocity characterizes the velocity of the consistent vortex bundle moving downstream and the fluctuation field is describing the chaotic velocity changes inside the bundle. The time average of the fluctuation part over a long enough interval is said to be zero.

The importance of different vortex length scales in turbulence was realised by Leonardo da Vinci in the 15th century and later, in direct connection to fluid dynamics research, by L.F. Richardson. Writing down the Navier-Stokes equations 1.3 with the use of the velocity fields obtained from the Reynolds decomposition leads to the Reynolds averaged Navier-stokes equations. Furthermore, the energy balance description of a turbulent flow may be derived as shown in [2]. The result is, that the energy is injected into the turbulent flow - fluctuation fields from the mean fluid flow in the form of large scale eddies (we can denote L as the characteristic length here). The dissipation of the turbulent energy occurs on small scales via effects of viscosity and its rate is given as:

$$\epsilon = \nu \langle \omega^2 \rangle \tag{1.6}$$

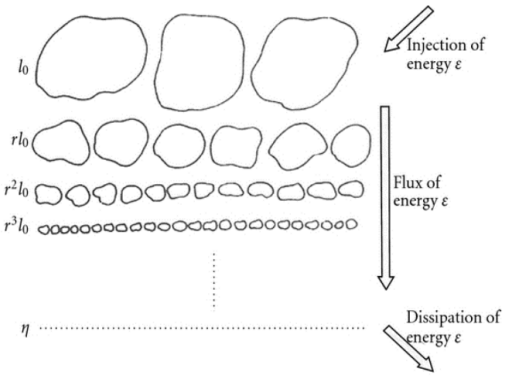

Figure 1.1: Richardson cascade.

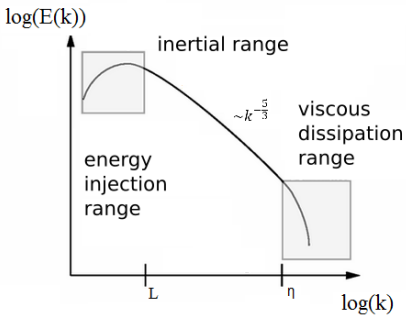

Figure 1.2: Kolmogorov's energy spectrum of turbulent flow.

where the circulation ω is given as $\nabla \times (\mathbf{v})$. Here, an open problem arises if one asks how the energy propagates between large and small scales.

The mechanism of energy transfer between large and small scales is called the Richardson cascade and states that the large eddies decompose to smaller and smaller scales through the cascade-like process shown in Figure 1.1. Furthermore, the ratio of the decrease in length scales is constant over the whole cascade and may be expressed as $l_n/l_{n+1} = const.$ The energy dissipation rate over the cascade is negligible. Here, the Reynolds number is an important parameter; it is proportional to a characteristic length scale, see 1.5 . For the large scale eddies created by the mean flow and for the vortex scales in the cascade, the Reynolds number is relatively high and the viscosity is less important for the fluid's behaviour. Only when sufficiently small scales are reached (Re$\sim$1) by the vortex decomposition process, the viscosity starts to cause energy dissipation, via the internal friction effects.

The most consistent theory discussing these properties of turbulent flows is Kolmogorov's theory [3]. It defines the Kolmogorov's dissipative length scale η [3] as the smallest length scale where the vortices are already stable in terms of the cascade processes. At this scale, the viscous dissipation of energy sets in.

$$\eta = \left(\frac{\nu^3}{\epsilon}\right)^{\frac{1}{4}} \tag{1.7}$$

Here, ϵ is the energy dissipation rate *-dE/dt* which in the steady state corresponds to the energy rate inserted to the turbulent flow. With all that was stated above, we can draw the shape of the energy spectrum *E(k)* in k-space as shown in Figure 1.2. It consists of the energy injection range for $k \leq 2\pi/L$ and the energy dissipation range for $k \geq 2\pi/\eta$ which, according to Kolmogorov, is determined only by ϵ and ν. The spectrum range in between these limits is called the inertial range and is determined only by ϵ. This assumption enabled Kolmogorov to derive

[3]The first Kolmogorov theory is known as K41 after the year in which it was presented. Two decades later, he published the K62 theory which includes corrections to his previous assumptions.

the following energy dependence in the inertial range by dimensional analysis:

$$E(k) = C\epsilon^{2/3}k^{-5/3} \tag{1.8}$$

with C being an universal constant.

1.2 Superfluidity

Both of the stable isotopes of a helium, ^{4}He and ^{3}He, undergo the second order transition to the superfluid phase at sufficiently low temperatures. Let us concentrate here on ^{4}He, for which the transition temperature to He II - its superfluid phase - is approximately 2.17 K, and can be easily reached by lowering the saturated vapour pressure above the helium bath [4]. In the superfluid state, quantum mechanical effects are seen at macroscopic scales, therefore we call these substances quantum fluids. This leads to unique and non-classical behaviour which was observed in many experiments during the second half of the previous century. Mainly, the thermal conductivity rises to be more than a million times larger than the normal state which allows for very effective heat transfer in the fluid, thus suppressing any boiling in the bulk. The experiments performed also showed that superfluid helium is able to flow without experiencing any viscous drag and that it creates a very thin superfluid film which perfectly wets almost every material. Furthermore, a direct connection between pressure and temperature gradients in superfluid helium has been found.

Over the years, different approaches to explain the unique behaviour of this state of matter have been used. At first, the connection with Bose-Einstein condensation was considered by London and further expanded upon by Tisza into what became the first two fluid model of superfluid helium. However, Landau had strong objections to their approach because all atomic interactions were neglected and the properties of an ideal bosonic gas were used. Landau's explanation of the superfluid state considered a gas of interacting quasiparticles, although it also worked on the two fluid nature of the substance. Today's knowledge shows that both approaches must be combined and that Bose-Einstein condensation really takes a part in the formation of a superfluid, but due to the interactions, the quantum mechanical ground state is composed of only cca. 10% of the condensate [4].

1.2.1 Two-fluid model

The two-fluid model is a phenomenological model which efficiently describes the extraordinary properties of superfluid helium - He II in the temperature range from the superfluid transition temperature (λ-point) down to ≈ 0.7 K. It states that He II consists of two inter-penetrating components, both having their own

[4]The transition temperature is three orders of magnitude lower for ^{3}He, at around 2 mK and it is technically more difficult to reach. It is done by diluting ^{3}He atoms in an isotopic mixture to pre-cool a spin 1/2 solid refrigerant before adiabatically demagnetising it tos sufficiently cool the ^{3}He. Bose-Einstein condensation in the case of superfluid ^{3}He manifests as the pairing (similar process as Cooper pairing of electrons in superconductors) of the fermionic ^{3}He atoms. Referring to the triplet or the singlet state of a pair of ^{3}He atom, two superfluid phases generally called A and B can be formed.

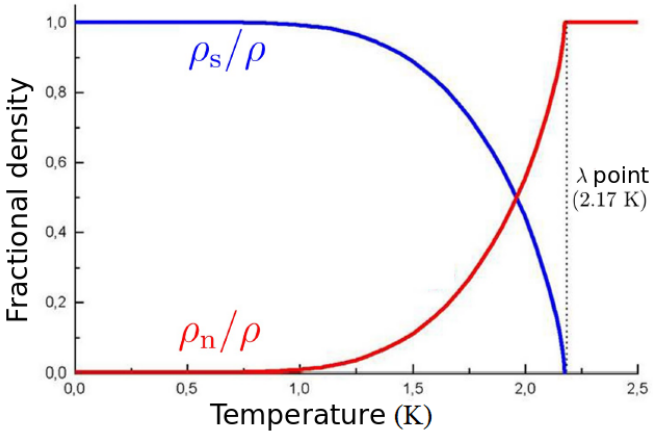

Figure 1.3: Temperature dependence of the normal (red) and the superfluid (blue) component density in a He II. The data originates from Andronikashvili's experiment with a stack of thin torsionally oscillating disks.

densities and independent velocity fields (this statement holds only for isothermal laminar flow). First, we will introduce the normal component with ρ_n and $\boldsymbol{v}_n$ being its density and its velocity field, respectively. The normal component behaves classically as a viscous fluid described by the Navier-Stokes equation 1.3 and is responsible for the distribution of all the entropy in the system. The superfluid component on the other hand can be described by Euler's equation 1.2 for an ideal fluid and has a density and velocity denoted as ρ_s and $\boldsymbol{v}_s$, respectively. Its lack of viscosity allows it to flow through the smallest gaps without any resistance and also allows for the creation of a superfluid film. The superfluid component carries no entropy at all, therefore its flow is said to be adiabatic.

The total density of He II is simply given as the sum of the two single component densities:

$$\rho = \rho_n + \rho_s. \tag{1.9}$$

The first considerations of the two-fluid nature of a He II originate from the Andronikashvili's experiment [5]. Torsional oscillator made from a set of a vertically-stacked, close-packed thin disks hanging on a string was fully submerged in superfluid helium, resulting in the temperature dependent swing period. The spacing between the disks was set to be smaller than the viscous penetration depth given as $\delta = \sqrt{2\eta/\Omega\rho_n}$, where η is the dynamic viscosity and Ω represents an angular frequency, therefore any normal component between the disks was trapped and moved together with the whole system. The satisfactory explanation of the swing period changes is that the ρ_n is changing with the temperature. Independent experiments also showed that the total density is roughly temperature independent. All this led to the determination of the temperature dependence of the normal and superfluid density ratios displayed in Figure 1.3.

A direct consequence of having two different velocity fields for the different components is the existence of flows without any equivalence in classical fluids. One of the flows without a classical counterpart is thermal counterflow, where the normal and superfluid components are moving against each other. In this

case, it is convenient to define the counterflow velocity as $\boldsymbol{v}_{ns} = \boldsymbol{v}_n - \boldsymbol{v}_s$. One possible and the most used method for driving counterflow is the creation of a temperature gradient resulting in a flow of the superfluid component towards the high temperature region, and of the normal component in the opposite direction to compensate for the gradient. Another non-classical He II flow is pure superflow, where the normal component is filtered by a superleak resulting in a flow of the superfluid component only. The third flow type is coflow, where both components are bound together and move jointly. All of the flows mentioned have their individual features and are worth detailed study.

1.2.2 Landau's theory of thermal excitations

Landau's theory was built on the fact that the weakly interacting fluid system can be interpreted as an ideal gas of elementary thermal excitations. Using his intuition, Landau was able to find the dispersion relations (the energy-momentum dependence), see Figure 1.4, for the excitations representing the normal component. The shape of the dispersion curve varies slightly with temperature and pressure. Here, it is shown as $E(\boldsymbol{k})$, where the momentum is given as $\boldsymbol{p} = h\boldsymbol{k}$. The low-energy linear part of the spectrum shown on Figure 1.4 represents the phonons with the dispersion relation [6]:

$$\epsilon = u_1 p, \tag{1.10}$$

with the speed of (first) sound u_1. The region around the local minimum for shorter wavelengths characterizes the roton part of the spectrum with the dispersion relation [6]:

$$\epsilon = \Delta + \frac{(p - p_0)^2}{\mu}. \tag{1.11}$$

Here, Δ represents the roton energy gap and μ is the roton's effective mass. The amount of thermal excitations in static He II rapidly decreases with the temperature, yet it is different for the phonons and the rotons. Thermodynamically, the dependencies can be found to correspond to Boltzmann's distribution and shows [6]:

$$N_f \sim (k_B T)^3, N_r \sim e^{-\frac{\Delta}{k_B T}}. \tag{1.12}$$

The roton population therefore decreases faster than that of the phonons and their contribution to the normal component at millikelvin temperatures is negligible. Phonons here are understood to behave similarly as those in solids, although due to the lack of a shear modulus in fluids, only longitudinal vibrations are to be considered. Today, rotons are understood to be a special case of phonons with a wavelength corresponding to the mean He II atom spacing.

The introduced theory of thermal excitations leads to the existence of a critical velocity which is given as $v_L = [\epsilon(p)/p]_{min} \approx 59\,\mathrm{m/s}$ [6]. By applying the Galilean transformation on the dispersion spectrum of moving He II, the spectrum gets tilted towards the $\epsilon = 0$ line. If any part of a spectrum gets below this line, the creation of excitations, meaning the creation of more normal fluid component, will start to be favourable, leading to the destruction of the superfluid state. Moreover, it is obvious that the first part of the spectrum to reach the negative energy will be the roton minimum. Therefore, the rotons are responsible for

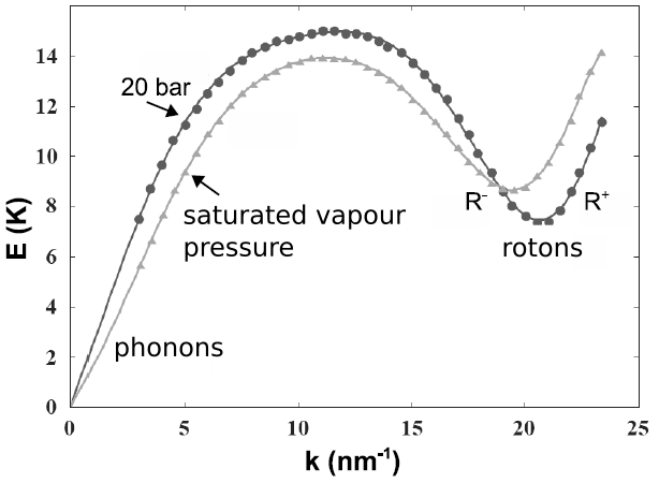

Figure 1.4: Dispersion spectrum of thermal excitations postulated by Landau. Linear part is due to phonons and the region of the local minimum characterizes the rotons.

the destruction of superfluidity above the critical velocity. However, in reality the generation of quantized vortices representing the instability of He II flow, which will be discussed later, onsets sooner than the Landau's critical velocity is reached.

1.2.3 Quantum mechanical approach

As previously stated, superfluid helium shows quantum mechanical behaviour at macroscopic scales. Therefore, Tisza established the macroscopic wave function description for He II.

$$\Psi(\mathbf{r}) = \Psi_0 e^{i\Phi(\mathbf{r})}, \tag{1.13}$$

It holds for the stationary state where Ψ_0 defines the wave function's amplitude and Φ its macroscopic phase. The presented description of He II leads to the following definition of the velocity of the superfluid component [7] given by the reduced Plank's constant $\hbar$ and the mass of the helium atom m_4 as:

$$\mathbf{v}_s = \frac{\hbar}{m_4}\nabla\Phi. \tag{1.14}$$

However, this equation directly leads to the restriction of any rotational structures in the flow of the superfluid component as $\nabla \times \mathbf{v}_s$ is identically zero. However, this conclusion was not in agreement with the experiments. It was later shown by Feynman [8] that vorticity is in fact allowed in the superfluid component but only with discrete quanta of circulation. The important fact here was that the wave function will not change if the macroscopic phase changes by $2\pi n$ with n being an integer. We can define the circulation for the superfluid component as follows;

$$\Gamma = \oint_L \mathbf{v}_s \mathbf{dl} = \frac{\hbar}{m_4}\oint_L \nabla\Phi \mathbf{dl} = \frac{\hbar}{m_4}(\Phi_f - \Phi_i) \tag{1.15}$$

Where Φ_i and Φ_f are respectively initial and final value of the macroscopic phase around a closed loop. For a multiply connected region with the knowledge that the wave function must not change after going around a closed loop L it can be shown that the circulation is quantised:

$$\Gamma = n\frac{\hbar}{m_4} = n\kappa, \tag{1.16}$$

with $\kappa = 9.997{\times}10^{-8}\ m^2/\mathrm{s}$ being the circulation quantum. Moreover, it is energetically favourable for each existing vortex to possess exactly one quantum of circulation. Therefore, all of the vortices in the superfluid component of He II are the same and we refer to them as quantized vortices.

1.2.4 Quantized vortices

The generation of quantized vortices is connected with the critical velocity (or angular velocity in the case of He II under rotation) of the superfluid component. Quantized vortices are taken as topological defects in He II, therefore they are bound to start and end at the He II surface or at the boundary of submerged bodies. In the bulk, they can exist exclusively in the form of closed loops. To fulfil the condition of a multiply connected region, there is no superfluid component at the centre of the vortex. The vortex core is Angström sized, and corresponds with the healing length over which the wave function can change its amplitude significantly. The velocity of the superfluid component is changing as *1/r* with the distance from the vortex centre. The structure of a quantized vortex and the spatial dependencies of ρ_s and $\boldsymbol{v}_s$ are shown in Figure 1.5. The energy per unit length of a vortex is basically the kinetic energy of the circulating superfluid component and given as [6]:

$$\epsilon_v = \int_{a_0}^{b} \pi\rho_s v_s^2 r dr = \frac{n^2\rho_s\kappa^2}{4\pi}\ln\frac{b}{a_0}. \tag{1.17}$$

Here, a_0 is the vortex core's radius and b is the dimension of the container. It clearly shows the favourability of singly quantized vortices as long as its energy grows as n^2.

A certain amount of vortices is already nucleated during the superfluid transition and they are very likely to be trapped in the protuberances of any submerged surfaces. With respect to the vortex core's dimension, practically every surface is relatively rough with a great amount of pinning centres and with respect to the assumption of the vortices' topology, it is highly unlikely that a pinned vortex will detach. Therefore, in almost every case, we have some remanent vortices, even in a stationary sample of He II. This leads to an extrinsic nucleation of vortices when He II is disturbed, with the remanent vortices working as seeding centres. The typical critical velocity for extrinsic nucleation is of the order of cm/s. It is however, possible to prepare a sample without remanent vortices if certain precautions are made. In such a case, the intrinsic nucleation of vortices may be obtained but at much the higher critical velocities of approximately 10 m/s.

The interaction between two parallel quantized vortices is dependent on their circulation's direction. In the case of a pair of vortices having the same direction of circulation, they will start to jointly rotate around their common centre. Vortices

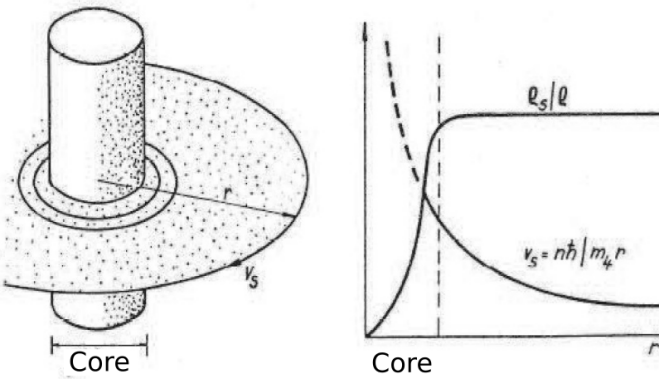

Figure 1.5: The structure of quantized vortex with ρ_s and $\boldsymbol{v}_s$ spatial dependencies. The dashed line represents the core's dimension.

with different directions of circulation will on the other hand move uniformly in a straight line in the same direction. The vortex loop may be considered here as a special realization of the second case, where every segment interacts with its opposite on the other side of the loop. As a result, the vortex loop is moving in the direction perpendicular to its plane with a velocity inversely proportional to its radius R given as [6]:

$$v_{loop} = \frac{\kappa}{4\pi R} \ln\left(\frac{8R}{a_0} - \frac{1}{4}\right). \tag{1.18}$$

1.3 Quantum turbulence

1.3.1 Dynamics of quantized vortices

Thus far we have been considering the dynamic behaviour of only two interacting quantized vortices, or of a vortex loop. For velocities well above the critical velocity for vortex nucleation, the amount of quantised vortices may be considerably large where the described system is becoming more complex. In such a case, we may talk about quantum turbulence which is generally a turbulent state of a quantum fluid. Quantum turbulence therefore consists of not only quantized vortices, but also the dynamical state of the normal component is relevant. For quantification, the amount of turbulence in the superfluid component the quantity called vortex line density L is used. It defines the total length of quantized vortices in a specific volume and is given in units of m^{-2}. Another useful quantity for describing quantum turbulence is the mean distance between quantized vortices l and is proportional to $1/\sqrt{L}$.

To describe a dynamical behaviour of quantized vortex interacting with normal and superfluid component flow we present the vortex equation of motion [6].

$$\mathbf{f} + \rho_s \kappa \hat{\kappa} \times (\mathbf{v}_L - \mathbf{v}_s) = 0 \tag{1.19}$$

The first term represents the force of mutual friction which originates from an interaction between quantized vortices and excitations which make up the normal component and will be discussed further in the following chapter. This term

therefore becomes negligible at very low temperatures - the limit of He II as a pure superfluid. The second term describes the Magnus force, where $\boldsymbol{v}_s$ is the flow velocity of the superfluid component, $\boldsymbol{v}_L$ is the vortex velocity perpendicular to its core and $\hat{\kappa}$ is the unit vector in the direction of the circulation.. It is seen from equation 1.19 that for very low temperatures the quantized vortex moves with the superfluid component and $\boldsymbol{v}_L = \boldsymbol{v}_s$.

The localized superfluid velocity for a given point r_0 on the vortex line can be determined by considering the following contributions. The first is the velocity induced at the desired point by the velocity fields of the same vortex as well as of other nearby vortices and is given by the Biot-Savart law 1.20 [7], in which the integration for the field is done for all quantized vortices present:

$$\mathbf{v}_s(\mathbf{r}_0) = \frac{\kappa}{4\pi} \int \frac{(\mathbf{r} - \mathbf{r}_0) \times d\mathbf{r}}{|\mathbf{r} - \mathbf{r}_0|^3} \tag{1.20}$$

This description of $\boldsymbol{v}_s$ points to an analogy with an electromagnetic field. This is hardly surprising if we consider that the superfluid velocity must obey the same assumptions of a potential $\nabla \times \mathbf{v}_s = 0$ and an incompressible flow $\nabla \cdot \mathbf{v}_s = 0$ as those given for magnetic induction in the stationary case of Maxwell's equations. The second contribution is due to an external velocity field and leads to the addition of a constant introduced by Schwarz in his equations for treating quantized vortex dynamics [9]. When the integration in equation 1.20 is done for a region close to r_0, one would obtain a singularity. In this case, a near field contribution of the local induction approximation (LIA) is used and leads to the self-induced superfluid velocity [7], which is given by the curvature radius of the quantized vortex at the point considered.

During the interaction of the quantized vortices with each other in the randomly oriented quantum turbulence, various forms of collision may happen. These collisions may result in a vortex reconnection where two meeting vortices may be split, which results in the exchange of their segments. This was observed in visualisation experiments [10] which tracked deuterium particles trapped on the quantised vortex core in He II flows. Another possible outcome of a vortex collision is the mutual annihilation of the quantized vortices. A vortex line may also be deformed by the interaction with another vortex or with the flow. This bend-like deformation with wave number k is then propagated along the vortex line in the form of a helical Kelvin wave as described in [11], with energy dependence $\omega \propto k^2$.

We have not yet discussed the energy dissipation mechanisms in quantum turbulence. It is expected that in the high temperature regime, which can be described by the two-fluid model, the viscous dissipation in the normal fluid is the dominant dissipative channel. Also, the superfluid component flow is affected by the normal component's behaviour via the mutual friction force, which allows the quantized vortices to imitate the normal component's flow. Experiments with classically generated quantum turbulence [12] (e.g., in a flow through a grid) showed the presence of the quasi-classical cascade-like process with the classical energy dependence 1.8 for the scales larger than the mean distance between quantized vortices l. Here, l is taking the role of Kolmogorov's length for the smallest scale of the cascade. The question here is, what is the dissipation mechanism in the absence of a normal component, i.e., in very low temperature limit? It was

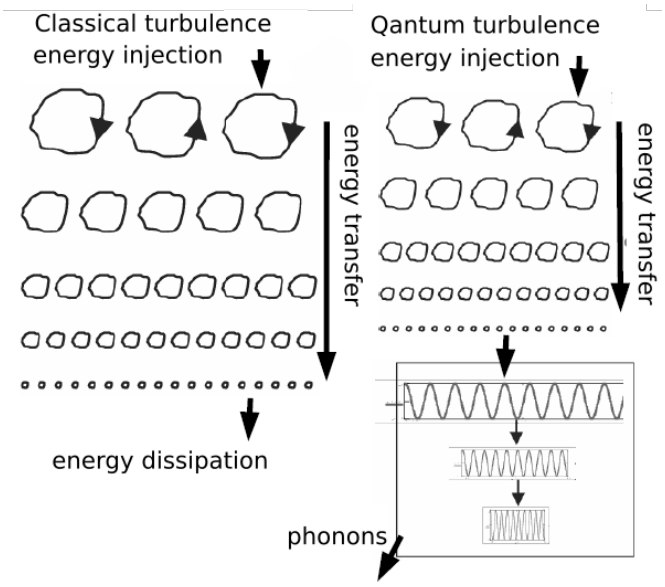

Figure 1.6: Energy cascade for classical turbulence (left) versus quasi-classical energy cascade continuing as Kelvin's waves cascade for quantum turbulence at very low temperature limit (right).

found in the experiments with quantum turbulence probed by ion bombardment at very low temperature [13], that the quasi-classical energy cascade, for scales below l, continues as a cascade of Kelvin's waves on individual quantized vortices. It is schematically shown in Figure 1.6. The turbulent energy is non-linearly propagated through the cascade towards the higher frequency region of Kelvin waves where it is radiated in the form of excitations representing the normal component (at the lowest temperatures, we are considering mainly phonons). The creation of normal component may be understood as a temperature rise, what points directly to the desired energy dissipation mechanism.

1.3.2 Different types of quantum turbulence

One of the first studied types of quantum turbulence was observed in Osborne's experiment [14] with a cylindrical container filled with superfluid helium rotating around its axis with angular velocity Ω. As a result, a matrix of parallel quantized vortices is created with a real vortex density $L = 2\Omega/\kappa$, as the superfluid component imitates solid body rotation. It was later shown that a two dimensional hexagonal matrix of vortices is the most favourable option which is stationary with respect to the rotating container's frame of reference, as is the case for vortices of magnetic flux in type-II superconductors. Analogically, there is also a lower critical angular velocity Ω_{c1} for which vortex nucleation starts to be energetically favourable and an upper critical angular velocity Ω_{c2} at which superfluidity should be destroyed, when vortex cores start to touch each other.

$$\Omega_{c1} = \frac{\kappa}{R^2} \ln \frac{R}{a_0}, \Omega_{c2} = \frac{\hbar}{m_4 a_0^2} \tag{1.21}$$

However Ω_{c2} is so large that it is practically unreachable.

Structurally, different types of quantum turbulence occur in mechanically driven He flows. One such flow is turbulence in bellows-driven flow past a grid. The two He II components are moving jointly (coflow) and they have the same velocity field on sufficiently large scales. Past the grid, homogeneous isotropic classical-like turbulence in the normal component is created with vortex structures on various length scales. The superfluid component is bound to the normal component via the mutual friction force and imitates its flow (similarly to how it imitates solid body rotation in the previously mentioned case), therefore we refer to this type of turbulence as quasi-classical. The classical-like energy spectrum in the inertial range $\sim k^{-5/3}$ was found experimentally [15]. Such an energy spectrum leads to the following of the temporal decay law [6] of quasi-classical turbulence.

$$L(t) = \frac{D(3C)^{\frac{3}{2}}}{2\pi\kappa\sqrt{\nu_{eff}}}(t + t^*)^{-\frac{3}{2}}. \tag{1.22}$$

Here D is the channel width, C is the constant from the inertial spectrum range and ν_{eff} is the effective viscosity of a quasi-classical fluid - which still has a two-fluid nature, but in first approximation behaves classically as a viscous fluid. The decay time is shifted here with the virtual time origin t^*, which gives the time of a virtual decay starting from an infinite value of the vortex line density. The steady state vortex line density grows with the flow velocity as $L \propto V^{\frac{3}{2}}$ [16]. This quasi-classical quantum turbulence with cascade-like energy transfer in the inertial range, classical energy spectrum (as was described in the previous subsection 1.3.1) and the temporal decay dependence $L \propto t^{-\frac{3}{2}}$ exists also in the very low temperature limit and is referred to the Kolmogorov type of quantum turbulence. Large initial vortex structures in the superfluid component can not be created by interactions with the normal component, but they can be created by a sudden stop in the rotation of a He II container, for example.

If quantum turbulence is generated non-classically, different properties are observed. This holds ,e.g., for turbulence created in thermal counterflow, where the velocity fields of the two fluid components are different for all length scales. The velocity of the counterflow $\boldsymbol{v}_{ns} = \boldsymbol{v}_n - \boldsymbol{v}_s$ is given by the applied heat power per unit area $\dot{q}$ as [6]:

$$v_{ns} = \frac{\dot{q}}{ST\rho_s}. \tag{1.23}$$

The characteristic structural attributes of such turbulence is the creation of a fully randomised tangle of quantized vortices which may be described by the Vinen equation [17]:

$$\frac{\partial L}{\partial t} = \alpha\chi_1 v_s L^{\frac{3}{2}} + g(v_{ns}) - \frac{\kappa}{2\pi}\chi_2 L^2. \tag{1.24}$$

The first term describes turbulence generation via the magnification of already existing vortex loops in the flow and the third represents the decay term due to the mutual annihilation of oppositely oriented vortex segments in a completely random tangle. The function $g(v_{ns})$ adjusts for the fact that no additional vortices except for the remnant ones are present at sub-critical velocities. Here α, χ_1 and χ_2 are constants. The resulting steady state vortex line density is proportional to the square of the counterflow velocity $L \propto V_{cf}^2$ [18], and therefore to the square of heat power applied. The Vinen equation leads to the temporal decay of the

turbulence described by following the equation [6].

$$L(t) = \frac{L_0}{t}. \tag{1.25}$$

The Vinen type of quantum turbulence described above was observed at very low temperatures in an experiment [13] where turbulence was generated by moving ions accelerated in an electric field. The random tangle created by interactions of the vortex loops generated was observed with the discussed properties of quantum turbulence.

1.4 Second Sound

1.4.1 Hydrodynamics of He II

The two fluid nature of He II results in a very unique and non classical hydrodynamic behaviour. In that case, the corresponding dynamical equations have to vary from the classical ones. The sets of equations for the normal and superfluid component are called the Hall-Vinen-Bekarevich-Khalatnikov (HVBK) equations and for an incompressible flow have the following form [7]:

$$\frac{\partial \mathbf{v}_n}{\partial t} + (\mathbf{v}_n \cdot \nabla)\mathbf{v}_n = -\frac{1}{\rho}\nabla P - \frac{\rho_s}{\rho_n} S\nabla T + \nu_n \triangle \mathbf{v}_n + \frac{\rho_s}{\rho}\mathbf{F}, \tag{1.26}$$

$$\frac{\partial \mathbf{v}_s}{\partial t} + (\mathbf{v}_s \cdot \nabla)\mathbf{v}_s = -\frac{1}{\rho}\nabla P + S\nabla T + \mathbf{T} - \frac{\rho_n}{\rho}\mathbf{F}. \tag{1.27}$$

The kinematic viscosity ν is of course used only for the normal fluid component. The quantity $\boldsymbol{F}$ represents the mutual friction force which in the presence of quantized vortices couples the velocity fields of the two fluid components. The vortex tension $\boldsymbol{T}$ is connected with the superfluid vorticity. Quantities P, T and S represent pressure, temperature and specific entropy, respectively. In the case of an isothermal flow without quantized vortices, the equation 1.26 simply changes to the Navier-Stokes equation for the normal component and the equation 1.27 to the Euler's equation for a superfluid component.

Due to the dynamic behaviour of He II, special wave modes are observable. New hydrodynamic equations allow for not only a classical sound wave (called first sound), in which the total density of the substance is oscillating and for which the wave propagation velocity can be derived [6] as:

$$u_1 = \sqrt{\left(\frac{\partial p}{\partial \rho}\right)_S}, \tag{1.28}$$

but for a second wave mode with the wave propagation velocity [6]:

$$u_2 = S\sqrt{\frac{\rho_s}{\rho_n}\left(\frac{\partial T}{\partial S}\right)_\rho}. \tag{1.29}$$

We refer to this mode as second sound. Unlike in first sound, the total density remains unchanged in the system. On the other hand, the density ratio of the two helium components varies locally while the normal and superfluid components

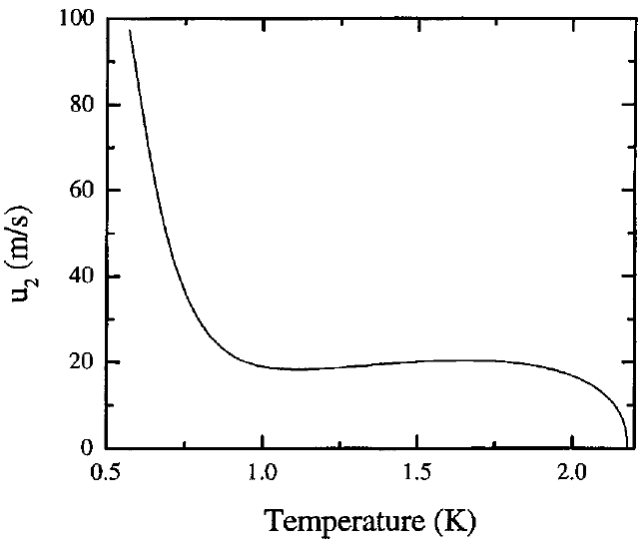

Figure 1.7: The temperature dependence of second sound velocity in superfluid helium at the saturated vapour pressure. There is a maximum of the second sound velocity at 1.65 K (in the region of the two-fluid model validity, T>1 K). At lower temperatures, the velocity is rising up to the value of $u_1/\sqrt{3}$. [20]

are oscillating in anti-phase. The oscillations of the component density ratio are directly related to temperature oscillations as implied by the two-fluid model, see 1.3. Therefore, the second sound wave can be interpreted as a temperature wave, and can thus be generated thermally. The temperature dependence of second sound velocity was characterized experimentally by Peshkov [19] and its values for given temperatures are listed in [20], where tabulated values for the temperature dependencies of all essential properties of liquid helium can also be found. The temperature dependence of the velocity of second sound is shown in Figure 1.7.

1.4.2 Mutual friction

If the velocity of superfluid helium rises so its flow starts transitioning from the laminar state to the turbulent state, then the velocity fields of the two He II components are no longer independent as the hydrodynamic equations 1.26 1.27 show. This is due to the fact that in the presence of quantized vorticity, the mutual friction force $\boldsymbol{F}$ term is no longer zero due to the scattering of the normal component's excitations off quantized vortices. A more complex phenomenological theory behind the mutual friction can be found in [21] obtained from the experiments with a matrix of parallel quantized vortices generated by the universal rotation of He II with angular velocity Ω. With the use of a coarse-grained description of such a system over length scales exceeding the mean inter-vortex distance l, the resulting analytical expression for mutual friction was presented in the following form:

$$\mathbf{F} = B\frac{\rho_n\rho_s}{\rho}\hat{\Omega}\times\Big(\Omega\times(\overline{\mathbf{v}}_s-\overline{\mathbf{v}}_n)\Big)+B'\frac{\rho_n\rho_s}{\rho}\Omega\times(\overline{\mathbf{v}}_s-\overline{\mathbf{v}}_n), \qquad (1.30)$$

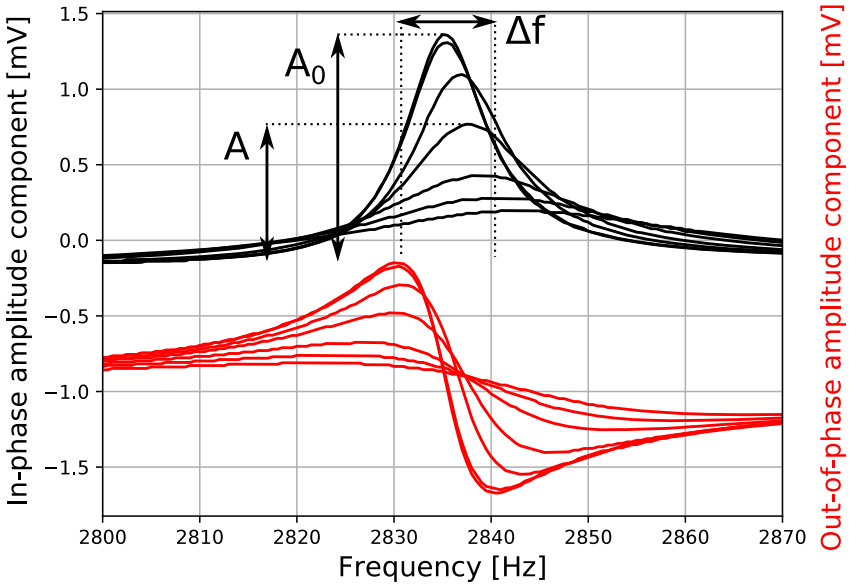

Figure 1.8: Series of second sound resonances measured for different vortex line densities in an experimental volume. The attenuation of the peaks grows with the turbulence intensity. The amplitude of the unattenuated peak A_0, its FWHM Δf and the amplitude of chosen attenuated peak A are highlighted in the figure. The frequency shift of the peaks is caused by temperature changes in the experimental volume, since the turbulence was generated thermally.

where B and B' are the experimentally determined mutual friction constants tabulated in [20], although the second term can be neglected in most cases. Unity vector $\hat{\Omega}$ is the direction of the angular velocity of the superfluid's rotation. The velocities of the normal $\overline{\mathbf{v}}_n$ and superfluid $\overline{\mathbf{v}}_s$ component have been averaged over an area containing a sufficient amount of quantized vortices. The equation 1.30 is pointing to the fact that a mutual friction force is trying to bind the velocity fields of the helium components together, its amplitude increases for larger differences between the normal and superfluid component flow velocities but is zero if they move together.

We have already presented second sound as an anti-phase oscillation of the two fluid components. The fact that a normal component is scattered on the quantized vortices means that the second sound wave should be strongly affected in the presence of quantum turbulence. The experiments with a standing wave of second sound across an area with a perpendicular matrix of quantized vortices (generated by universal rotation) have been conducted by Hall and Vinen [21]. As a result, the amplitude of the second sound standing wave was strongly attenuated by increasing the amount of quantized vortices present in its path. But this was only true when the vortices in the matrix have been perpendicularly oriented with respect to the direction of wave propagation. In the case where the second sound wave was oriented along the vortices, no attenuation was observed. It was then shown that the normal component is scattered on quantized vortices, but the scattering cross section is strongly angularly dependent.

An essential method of determining the vortex line density was developed on the previously described principle. Lorentzian peaks of the second sound resonance are sequentially measured and the attenuation of their amplitude A is obtained with respect to the amplitude A_0 of an unattenuated peak, i.e, in the absence of any quantized vorticity. The illustrative series of measured second sound resonant peaks with different attenuation level is shown on Figure 1.8. The corresponding vortex line densities are then calculated using the following equation [12]:

$$L = \frac{6\pi\Delta f}{\kappa B}\left(\frac{A}{A_0} - 1\right). \tag{1.31}$$

Here, Δf is the width (FWHM) of the unattenuated peak, κ is the circulation quantum and B is the mutual friction constant. Although the presented equation is derived from the concept of quantum turbulence in the form of a fully random tangle of quantized vortices, the obtained vortex line densities may therefore vary from the exact values if a differently structured quantum turbulence is studied. The maximum uncertainty resulting from using equation 1.31 to determine the vortex line density in an experiment is estimated to be 33%.

2. Experimental apparatus

2.1 Low temperature and vacuum technique

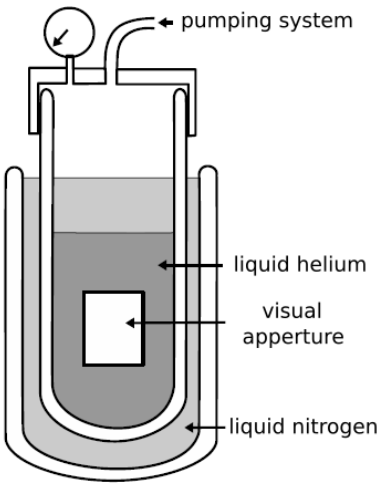

Figure 2.1: Schematic of the glass cryostat.

To obtain sufficiently low temperatures, an efficient pumping system and good thermal isolation is needed. All of our experiments are performed in the two-fluid regime, therefore the cool-down technique of lowering the saturated vapour pressure above the helium bath was used. Testing and optimization measurements have been executed in a small glass cryostat, schematically shown in Figure 2.1, with an inner diameter of 60 mm and volume of cca. 2 litres. The helium container, sealed and connected to the pumping system, is made of double-walled glass with vacuum in between for thermal isolation and is coated with a reflective silver layer (only a small stripe is left uncoated as a visual aperture). Around it, a similar double-walled glass container is used for liquid nitrogen. Liquid Nitrogen is used here for pre-cooling (to lower the helium consumption during an experimental insert cool-down) and to decrease the radiative heat-leak into the helium bath, which depends on the outside temperature as T^4, according to the Stefan-Boltzmann law. The liquid helium is provided by a liquefier housed in the same building as the superfluidity laboratory, therefore all of the helium evaporated in the experiment can be collected by a recovery pipeline and sent back for re-liquefaction. Liquid helium, with a boiling temperature of 4.2 K, is transferred into the cryostat through the double-walled stainless steel siphon by the slight over-pressure of a transport Dewar. The approximative value of the temperature of the helium bath is obtained from saturated vapour pressure measurements using a MKS Baratron pressure gauge with the range of 0 to 1000 Torr and determined with the use of its tabular values given in [20]. The pressure corresponding to the λ-transition temperature is slightly below 38 Torr.

The systematic measurement of the proposed studies has been executed in a bigger cryostat with inner volume of 70 litres. The helium container is made from stainless steel, and is connected to the top flange via a plastic neck. Unlike the small glass cryostat, there is no nitrogen bath. The thermal isolation of this steel dewar is more efficient and pre-cooling is done either by directly filling the cryostat with liquid nitrogen, which is syphoned out afterwards or simply by cold helium gas from a transport Dewar. Assuming relatively stable helium consumption throughout the experiment, it should continuously run for around five days before a liquid helium refill was needed. The experimental cell was placed right above the bottom of the cryostat to ensure the longest possible measuring time. For the in-situ temperature measurements of the helium bath, a semiconductor resistive thermometer (MicroSensor TTR-L) made of Ge on an GaAs film enclosed in a copper capsule placed near the experimental cell was used.

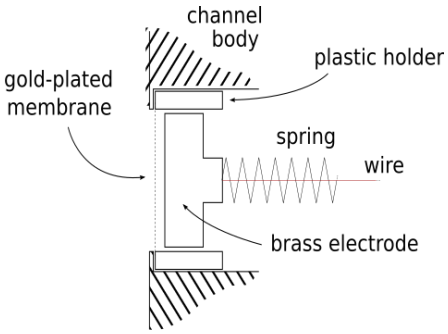

Figure 2.2: A capacitive second sound sensor consisting of a nuclepore membrane coated with a thin golden layer. The membrane is stretched in the teflon holder and a brass electrode is pressed against it. DC voltage applied to the channel's body induces the bias and the membrane movement is driven by an AC voltage applied to the electrode.

The resistivity range of the thermometer for the observed temperatures was from 140 Ω at room temperature to cca. 10 kΩ for the lowest temperatures reached. The calibration of the thermometer was done with respect to the simultaneous measurement of the saturated vapour pressure with the MKS Baratron, which were converted to temperature using the HEPAK program [22]. To pump the vapours above the helium level, an oil-sealed Roots pump was used which allowed us to obtain temperatures as low as 1.3 K in this configuration.

2.2 Second sound sensors

Measurement of second sound attenuation is a standard detection technique [18] for the quantification of the amount of quantized vortices in the two-fluid regime. The amplitude of a second sound standing wave in a resonator is attenuated in the presence of quantized vortices in the probed region due to the scattering of the normal component on the vortex cores. The standing wave of second sound in the resonator may be generated mechanically by an oscillating superleak. The superfluid component is not affected by the superleak movement due to lack of viscosity. On the other hand, the superleak introduces a solid wall for the normal component, causing longitudinal oscillations with the frequency of the wall's movement. As a result, the local changes of the componential density ratio is observed in the form of a standing wave. The amplitude of the wave is resonantly amplified if the superleak movement frequency is close to the resonator's natural frequency mode. Another movable superleak on the other side of the resonator may be used for the detection of a transmitted wave, if the position of the superleak during its induced oscillations may be determined.

We have used capacitative second sound sensors, which are schematically presented in Figure 2.2 and represent the standard devices used in our laboratory. A photography of a typical sensor, which provides a closer look at its construction, is shown in Figure 2.3. The second sound sensor consists of a nuclepore membrane, which acts as a superleak and is coated with a 30 nm to 100 nm golden layer for electric conductance. The membrane is stretched across the circular teflon

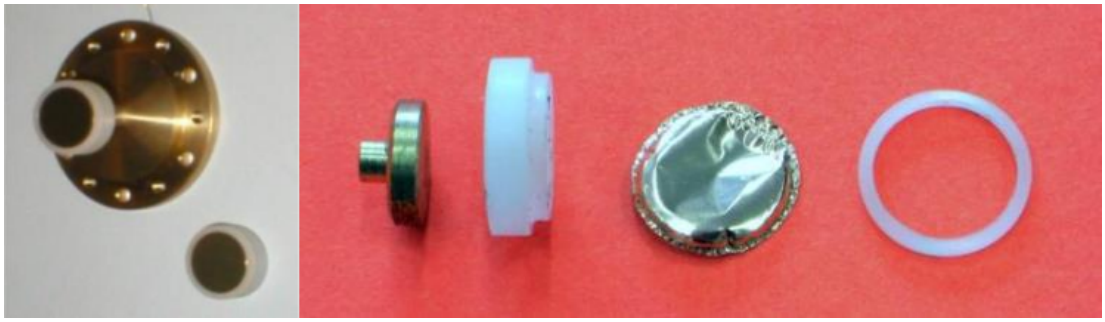

Figure 2.3: Photograph of a fully built second sound sensor (left) prepared for installation into the experimental channel. A decomposed sensor (right) made from a brass electrode, teflon holder and gold-coated nuclepore membrane (from left to right, respectively).

holder with a diameter of 1 cm and is connected to the channel body. The brass electrode is pressed with a spring against the uncoated side of the membrane. By applying a DC voltage (typically 100 V) to the channel's body, a bias is created between the membrane and the electrode. For such a device, the ideal capacitance is in the range 30 to 100 pF. If an AC voltage is applied to the electrode, the changes in the bias will cause the membrane to move with the frequency supplied by voltage generator. Quantum turbulence detection unit is made of two sensors, such as those described, facing each other. One works as a transmitter, where an AC voltage is applied to it causing the membrane to oscillate and the other is used as a signal reader, where the induced membrane oscillations are transformed into an AC voltage read by a phase-sensitive lock-in amplifier referenced at the frequency of the AC voltage generator.

2.3 Experimental cell

The experimental volume is represented by the 1 cm wide channel of square cross-section inside the brass cell, shown in Figure 2.4. The channel is 3.2 cm long with polished walls closed on both sides (but not leak tight) and represents the second sound resonator. Two different second sound signals have been used in the experiment. One was generated with low amplitude between two second sound sensors of the type described in the previous section. These sensors were placed in the centre of the channel perpendicular to its long axis, as shown in the schematic sketch of the experimental cell in Figure 2.4. The generated signal was used for quantum turbulence detection. The other (high amplitude) second sound signal that was used for turbulence production, was generated along the channel via the resistive heater. The frequencies of the modes used were far enough from each other to eliminate any possible crosstalk between the two signals.

The heater was made from Manganin resistive wire with resistance of 50 Ω to ensure an impedance match with the generator used. The manganin wire was mounted on a Stycast paper platform in a zig-zag pattern and was held in place by a couple of small drops of varnish. It was placed at the end of the brass holder, loosely fitted in the channel. A standing temperature wave, i.e. second

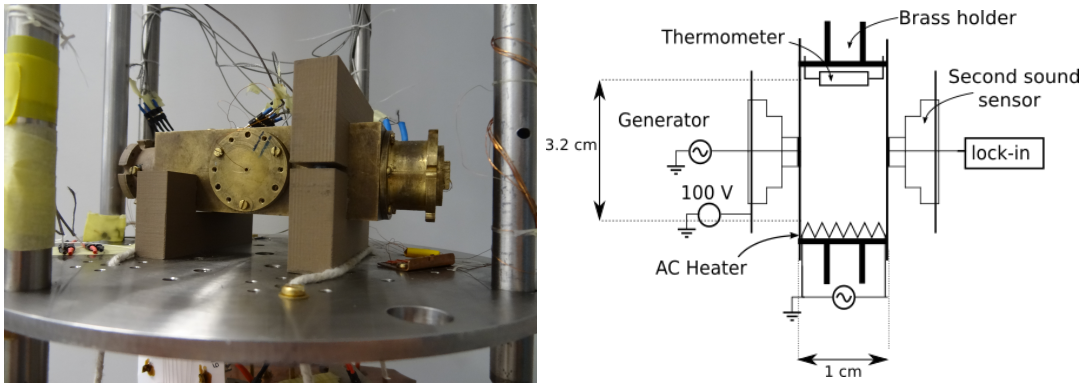

Figure 2.4: Left: Photograph of the experimental cell with the second sound sensor holder on the front side. The heater and the thermometer used for longitudinal second sound modes have been placed on the brass holders and inserted into the channel from left and right side with resulting spacing of 3.2 cm. Right: Schematic of the experimental cell arrangement. One second sound signal was created between the two capacitative sensors placed in the centre of channel perpendicularly to its length and used for turbulence detection. The other second sound signal was generated along the channel by resistive heater and was probed by a thermometer on the other side of the channel. This signal was used for the generation of quantum turbulence.

sound wave, was generated as an AC voltage was applied to the heater. However, the radiated thermal power is proportional to the square of the applied voltage which leads to a temperature wave with a frequency double to that provided by the generator. The temperature oscillations observed on the other side of the channel were measured by a resistive Ge/GaAs thermometer, similar to the one used for the bath temperature measurements, but without the copper capsule resulting in faster thermalisation. This thermometer was also placed on a Stycast paper platform at the end of the brass cell. Optimisation measurements showed that the thermally non-conductive walls of Stycast paper placed behind the heater and thermometer have improved the second sound resonator's quality. The thermometer was supplied with a constant current of 1 μA, and the resistance changes, induced by temperature changes, have been measured as a voltage signal by a phase-sensitive lock-in amplifier. From the largest changes measured in the thermometer's resistance, we estimate the maximum amplitude of the temperature waves generated to be of the order of millikelvins.

2.4 Temperature control

A great amount of superfluid helium's properties are strongly dependent on temperature as Ref. [20] shows. Therefore, temperature control is essential for any systematic experiments. Manual temperature stabilisation via the mechanical control of the pump's valve is not ideal. This is because the system's reaction to any such change is very slow and there is bad resolution of the possible pressure changes. Automated electrical temperature stabilisation is more suitable. A pumping rate faster than what would be needed for a chosen temperature stabilisation is maintained and additional heat power is applied the helium bath via the

resistive heater driven by the DC voltage generator. The heat power produced by the heater is regulated with a PID (proportional integral derivative) control feedback loop programmed in the LabView environment. Immediate values of the heat power *h(t)* to be applied are given by equation 2.1 from the temporal development of an error value *e(t)* which is given as the difference of the actual value and a set value of the stabilized quantity (for us it is the temperature).

$$h(t) = P.e(t) + I.\int_0^t e(t)dt + D.\frac{de(t)}{dt}. \tag{2.1}$$

The first term represents the current error value and changes rapidly with it, the second integral term involves the history of the error value and the last derivative term is trying to predict the future development of the error value. Coefficients P, I and D are always positive, and represent the weights of the corresponding terms. The change of the coefficient's values affects the stabilisation quality and its relaxation time. For example; if I is over-estimated, the feedback will be slow and will result in damped oscillations around the set value. The same would happen if the temperature will be regulated from a value which is far from the set-point as the integral part would grow large (either negative or positive if we regulate from higher or lower values, respectively). In that case, the possibility of clearing the integral term to zero as the set-point is approached is convenient. We have been using the values of P between 10 and 100, the values of I between 1 and 10 and we have been keeping the value of D equal to zero. The resulting temperature stability achieved in all experiments was in the order of tenths of millikelvins.

3. Results

3.1 Second sound resonances

3.1.1 Transversal spectrum

Our experiment was based on two perpendicular second sound signals. We refer to them as to the transversal second sound mode and the longitudinal second sound mode. The transversal mode was used for quantum turbulence detection and driven at low amplitude between two capacitative second sound sensors of the type described in the previous chapter 2.2 with a resonator of dimension $d_T = 1$ cm (width of experimental channel). The measured spectrum of the transversal second sound resonances in the frequency range 300 Hz to 18 kHz is shown in Figure 3.1. It displays a non-systematic rise of the peak's maximum with the frequency, where the first harmonic resonance, with a resonant frequency of around 1 kHz is hardly measurable. The frequency of the first resonant mode is given by the second sound velocity v_{SS} and the dimension of the resonator as $f_0 = v_{SS}/2d_T$. Higher harmonic modes are then the integer multiples of the first resonant frequency. Figure 3.1 also shows that the phase of even harmonic modes is π-shifted from the phase of the odd ones. This feature is typical for second sound spectra [18]. The reason for this peak inversion is, that in the case of even harmonics, the oscillation of the detection membrane is out of phase with the driving membrane.

Another typical feature of second sound spectra is the temperature dependence of its resonant frequencies. This is caused by the temperature dependence of the second sound velocity displayed in Figure 1.7 which has a maximum at 1.65 K. The resonances for higher as well as lower temperatures are shifted towards lower frequencies as may be seen in the inset of Figure 3.1. The described features are therefore typically used to confirm that any peak measured is actually a second sound resonance.

For each temperature, we have chosen only one second sound resonant peak whose attenuation was then used for quantum turbulence detection. One of the criteria for the suitability of a given peak was a high quality factor $Q = f/\Delta_f$. We have obtained quality factors of the order of 150 in our experiment. Another criterion was high peak amplitude to better resolve its attenuation. And finally, we choose lower harmonic modes because to reduce the effect of frequency shifts of the second sound peaks, relative to their position, due to overheating. However, the frequencies used were still at least ten times higher than the frequencies of the other second sound signal generated in the perpendicular direction. This ensured the suppression of any possible signal coupling.

When high power was applied to the channel heater, overheating of the experimental volume could occur, which would cause a shift in the second sound resonance frequency. We have therefore used a measurement of the complex amplitude components (absorption and dispersion signals) for the reconstruction of the actual second sound amplitude at resonance, when performing time-resolved measurements on a fixed frequency (initially set to the resonant one). The amplitude corrections were necessary, if the second sound peak had been shifted

significantly due to overheating. Further discussion on this subject may be found in following chapter.

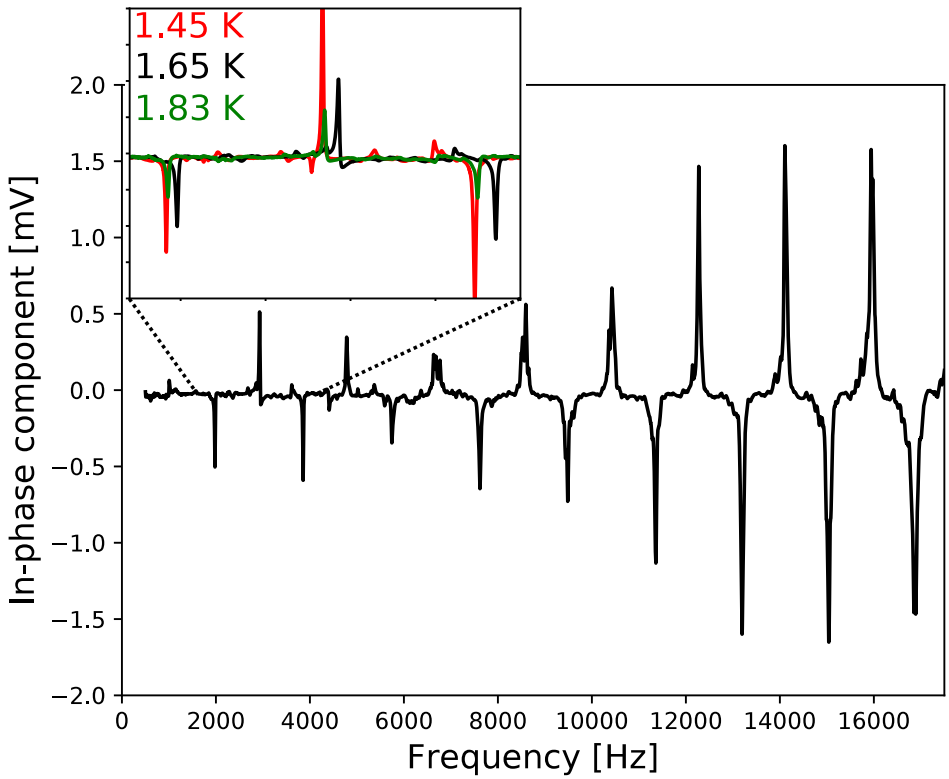

Figure 3.1: Frequency spectrum of the second sound signal in the range 300 Hz to 18 kHz at 1.65 K. A second sound wave was generated transversally with low amplitude between two capacitative second sound sensors. The expected position of the first resonant frequency is 1018 Hz, based on the second sound velocity value of 20.36 m/s (at 1.65 K) [20] and a resonator dimension of 1 cm. The plot presented shows the position of the fist harmonic slightly below 1 kHz, which points towards a slightly larger effective length of resonator (caused by imperfect positioning of the sensors and non-zero velocity at the membranes). All of the higher harmonics are integer multiples of the first resonant frequency. The spectrum shows the characteristic feature of phase inversion for all even harmonic modes. The temperature shift of the resonances for the different temperatures (caused by second sound velocity changes) may be seen in the inset. Both 1.45 K and 1.83 K are shifted towards the lower frequencies which agrees with the second sound velocity temperature dependence shown in Figure 1.7.

3.1.2 Longitudinal spectrum

The longitudinal dimension of the second sound resonator represented by the closed brass channel was $d_L = 3.2$ cm. This dimension leads to an estimate of the first harmonic resonant frequency of around 300 Hz. However, the longitudinal second sound signal with high amplitude was generated with a resistive heater

driven by AC voltage. As a result, the actual second sound wave frequency was double that supplied by the voltage generator, as described in the previous chapter. In our experiments, we focused on the first three harmonic modes of the longitudinal second sound signal. These modes are geometrically illustrated in Figure 3.2. Individual harmonic modes differ from each other in the number and position of their nodes and anti-nodes. All of the odd harmonics have an anti-node in the centre of the channel whereas for the even harmonics, the node lies in the centre. The anti-node of the second sound standing wave represents the position with the maximum amplitude of the oscillatory motion of the superfluid helium components against one another. On the other hand, in the node, the component density ratio remains unchanged, resulting in zero counterflow velocity. Thus, we expect spatial localisation of the generation of quantum turbulence in the wave's anti-node, for which we have maximal counterflow velocity. Therefore, the amount of quantized vortices observed in the centre of the channel should differ for each resonant mode. Specifically, for low frequency even harmonics, we should not see any turbulence generation in the channel's centre.

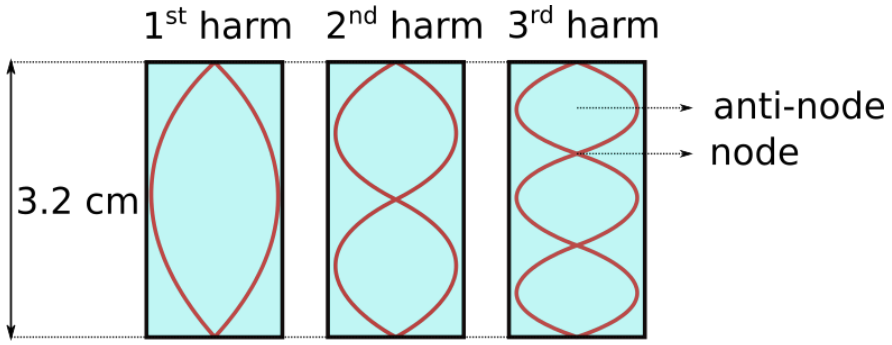

Figure 3.2: Geometry of the first three longitudinal second sound harmonic modes. The red curves display the amplitude of the oscillatory motion of the two fluid components against each other. In the centre of the channel, for odd harmonics, there is a wave anti-node, where velocity amplitude is maximal. For even harmonics, a wave node is positioned in the centre of channel, for which no componential density ratio changes occur.

The longitudinal second sound spectrum, including the first three harmonics, is shown in Figure 3.3. The frequency axis represents the frequency of the voltage generator. Therefore, the first harmonic resonance is actually around 300 Hz. The phase inversion of the even peaks is also visible for the longitudinal spectrum. Furthermore, the difference of the resonant frequencies at different temperatures may be also seen. However, in absolute values, the frequency shifts are much smaller in this frequency range. One needs to bear in mind that the spectrum shown in Figure 3.3 is measured in the laminar regime where no significant amount of quantized vortices were created. Cases where the longitudinal second sound signal was used for the generation of quantum turbulence will be discussed later.

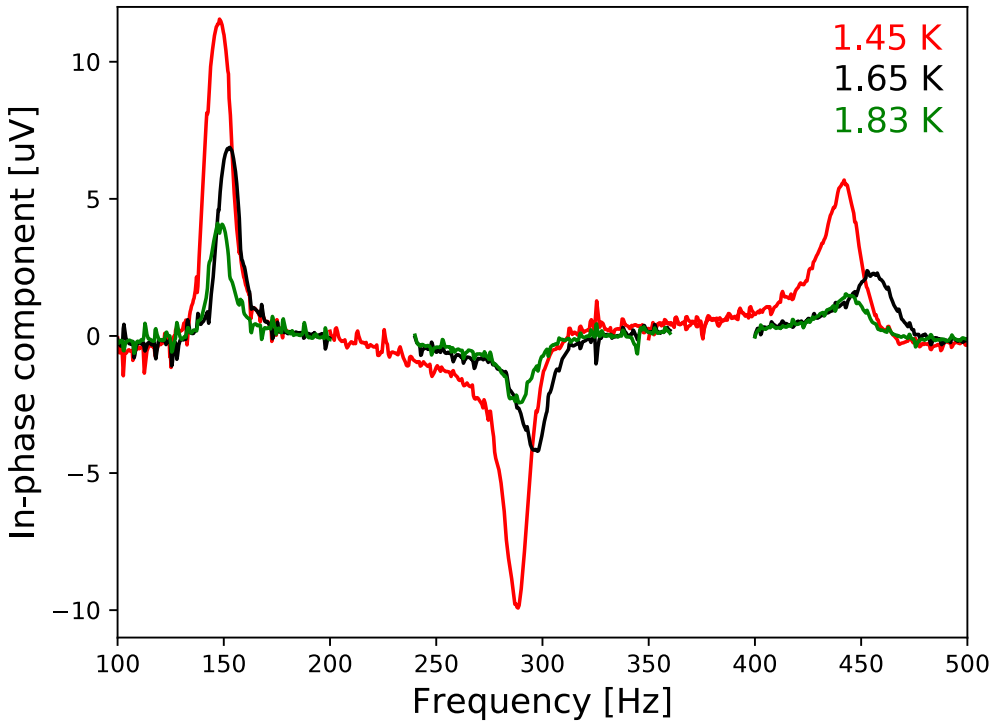

Figure 3.3: Frequency spectrum of the longitudinal second sound signal generated at high amplitudes. The first three harmonic modes are shown for all measured temperatures. The actual frequencies of the second sound wave are double than those displayed as horizontal axis represents the frequencies set on a voltage generator. The frequency shift for different temperatures is significantly lower (in absolute values) than those of the transverse mode due to lower resonant frequencies. Again, the frequency shifts correspond to the temperature dependence of the second sound velocity.

3.2 Quantum turbulence generation

Here, we have repeated the quantum turbulence generation experiment of Kotsubo and Swift [23] with a thermally generated standing wave of second sound. We also include a study of the amount of vortices generated as well as characterisation of the decay of such turbulence. To his end, we measured full resonant peak series for various driving powers of the resistive heater generating the longitudinal second sound wave. Measurements were performed at three different temperatures, 1.83 K, 1.65 K and 1.45 K for the first three harmonic modes. The resonant peaks were measured by the thermometer biased by a DC current of 1 μA, as described in chapter 2.3 in the form of frequency sweeps with a resolution of 0.3 Hz. Heating powers were in the range 4 mW to 200 mW. The actual driving power was determined from the direct measurements of the voltage on the heater and of the current running through it during a sweep measurement.

Frequency sweeps for the first harmonic mode and for the other two harmonic modes at 1.45 K are shown in Figure 3.4 and in Figure 3.5, respectively.

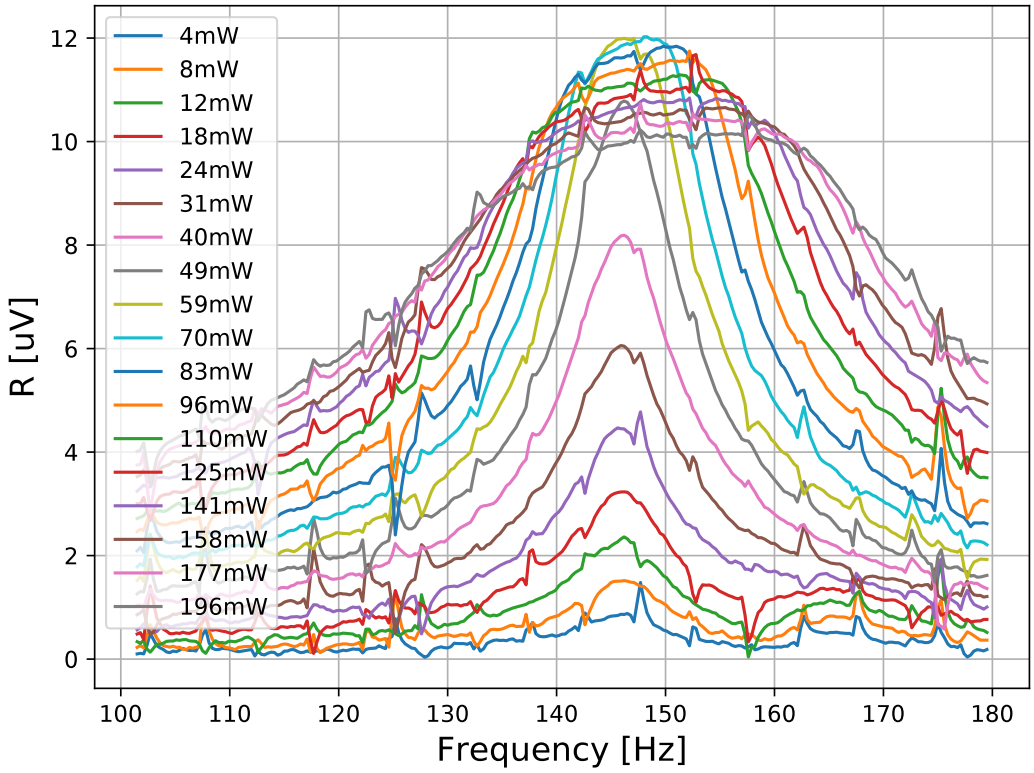

Figure 3.4: Frequency sweeps of the first longitudinal harmonic at the various indicated heating powers. Horizontal axis represents the frequency supplied by the voltage generator (half the second sound of frequency). On the vertical axis, we show the amplitude of the voltage response of thermometer. Two different regimes can be clearly seen; A low power regime with Lorentzian-like resonant peaks indicating laminar oscillatory flow and a high power regime with the saturation of the peak amplitude. Amplitude saturation points towards the generation of quantized vortices which cause the second sound peak to become attenuated.

The results obtained are in agreement with the previous experiment [23]. We have observed two regimes: One for the low powers where all of the resonances have Lorentzian shape. This indicates that the oscillatory flow studied here is in the laminar regime. The amplitude of the resonant peaks increases linearly with increased heat power in this regime. For high heat powers (above some critical value), the resonant behaviour is significantly different. The peak amplitude saturates within the high power regime and the tops of the measured peaks appear as if they were cut. Although, the peak amplitude is not rising anymore with the power in this regime, the resonances are still getting broader. Turbulence is generated over a wider frequency range around the resonant frequency at these higher powers. The existence of a saturated peak amplitude points towards the existence of a critical flow velocity needed for quantized vortex generation. The fact that the saturated value of the amplitude decreases with increased power is not in agreement with Kotsubo's experiment and will be discussed later. This behaviour is similar for all three of the longitudinal second sound harmonics used, as may be seen in Figures 3.4 3.5. However, in the case of the third harmonic,

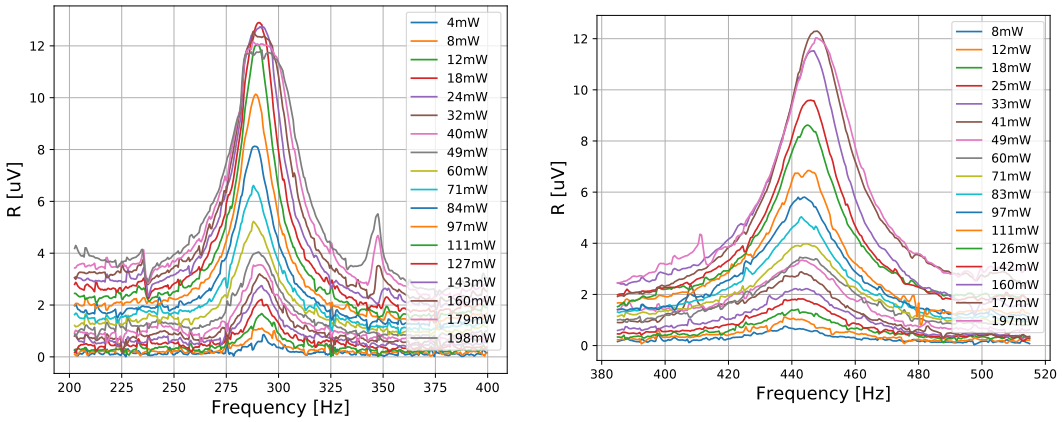

Figure 3.5: Resonant peak series of the second harmonic (left) and the third harmonic (right) of the longitudinal second sound standing wave. The series was made with use of the different heat powers. The horizontal axis represents the frequency of the voltage generator. On the vertical axis, we show the value of the amplitude of the voltage response of the thermometer. Obtained behaviour is similar as for the first harmonic mode. However, in case of the third harmonic, the change of the peak's shape may be seen only for the highest heat power.

the non-Lorentzian shaped peak was observed only for the highest heat power used. But, this peak does not display the flat-top indicating the development of turbulence. The limiting heat power of the apparatus is therefore on the edge of the critical power for the third harmonic mode at 1.45 K. We have observed similar behaviour at the other investigated temperatures and with even higher critical powers for the harmonics considered.

3.3 Steady state turbulence

Amplitude saturation of the longitudinal second sound indicates the generation of quantized vortices. However, the transverse second sound signal gives us the possibility to prove this hypothesis and furthermore, to quantify the amount of vortices created. Therefore, we performed simultaneous measurements of the attenuation of the transversal second sound signal (in the form of a time trace of the transversal second sound amplitude at a fixed frequency) along with the longitudinal sweep measurements described in the previous section. The results obtained are presented in Figure 3.6.

We chose the optimal transversal peak and found its resonant frequency at a given temperature. The driving second sound membrane was kept at its resonant frequency during the whole longitudinal sweep measurement. Such measurements were done for all used heat powers and for all studied temperatures. To illustrate the principle, we have chosen some of the different heat power measurements with the first longitudinal harmonic at 1.45 K and display them in Figure 3.6. We see that for the laminar - low power regime - no significant attenuation of the transversal signal occurs. The visible decrease of the transversal signal can be clearly connected with the saturation of the longitudinal signal amplitude. This clearly proves that quantum turbulence may be generated if the longitudinal

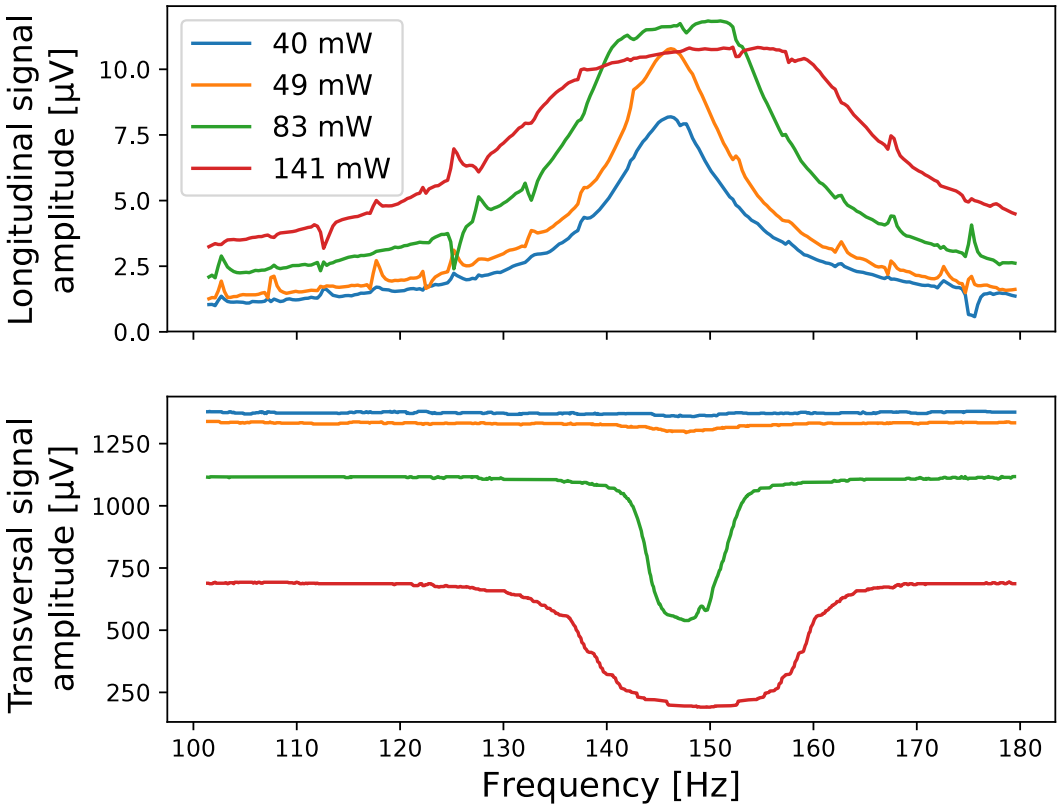

Figure 3.6: Top: Selected frequency sweeps for the first longitudinal harmonic at 1.45 K at the various indicated heating powers. The peaks presented represent both laminar (low power) and turbulent (high power) regimes. Horizontal axis displays the frequency of the generator and the vertical axis shows the amplitude of the measured longitudinal signal. Bottom: Amplitude of the transversal second sound measured simultaneously with longitudinal sweeps. Transversal signal was held on resonance. The horizontal axis was modified so the transversal signal amplitude directly corresponds to the longitudinal frequency. The attenuation of the transversal signal clearly corresponds to the saturation of the longitudinal signal's amplitude.

second sound is intense enough. Also, it shows that the quantized vortices start to be generated exactly when the longitudinal second sound amplitude saturates, suggesting the existence of a critical velocity. Next, the turbulence generated grows denser as the longitudinal signal nears the resonance.

We have obtained the power evolution of the second sound peak amplitude for all three longitudinal harmonic modes at 1.45 K and show them in Figure 3.7. It was done to better display the characteristic features of quantum turbulence generated in the steady state. The values of the peak amplitude in high power region (non-Lorentzian shape of peaks) were determined from full sweeps as an average value of 7 data points around the maximum of the amplitude of thermometer's voltage response R (the mere value of the maximum was in some cases not adequate due to parasitic oscillations in the measured peaks).

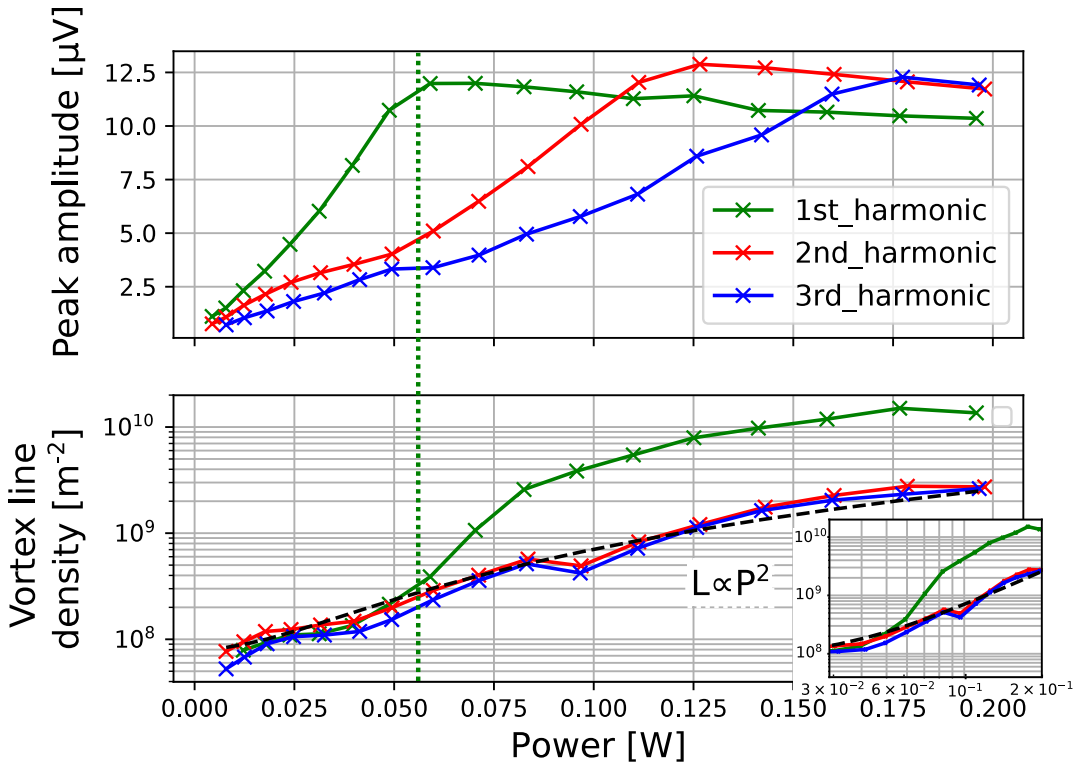

Figure 3.7: Top: Power evolution of the second sound peak amplitude for all three longitudinal harmonic modes at 1.45 K. The critical counterflow velocity for which the transition to the turbulent state occurs was observed for all harmonics (although, for the third harmonic mode (blue), it is on the edge of the limiting heat power). Bottom: Corresponding vortex line densities measured in the centre of the channel via attenuation of the transversal signal. The black dotted line displays the theoretical amount of the background vortex line density originating from the DC counterflow which scales as $L \propto V_{cf}^2$ (see text). A closer look on this scaling for power region of 30-200 mW is shown in the inset in the form of log-log plot. The green vertical dotted line shows the critical power for the first harmonic mode. Both the longitudinal and transversal signal imply the additional generation of quantized vortices in the anti-node of the second sound standing wave above this critical value. No additional increase in the vortex line density for the second harmonic mode confirms the anti-nodal localisation of vortex generation.

The top panel of Figure 3.7 shows that all three harmonic modes have similar behaviour. The dependence of the second sound peak amplitude with heating power is linear in the laminar regime. Power applied to the heater is directly proportional (it differs by the temperature-dependent factor $1/\mathrm{ST}\rho_s$) to the DC counterflow velocity V_{cf} given by equation 1.23. The critical powers (connected with critical velocities), for which the amplitude saturation occurs were found for all three harmonic modes at 1.45 K. However, for the third harmonic mode, it is on the edge of the limiting heat power (as discussed in previous section)

and the fully developed turbulent regime was not observed. We were not able to reach the critical power for all harmonic modes at higher temperatures, as they shifted beyond the value of the limiting power (∼200 mW) given by the voltage generator. Furthermore, the saturated value of the peak amplitude is, in the turbulent regime, decreasing as the heat power increases. It is most probably connected with the additional turbulence in DC counterflow. The dependence of the critical power (i.e., velocity of studied counterflow) on the number of used harmonic is not yet fully understood and will be further discussed in the following chapter. Finally, the results obtained here are similar to those obtained at the other two temperatures.

We have estimated the values of critical heat power from the data obtained at the different temperatures for different harmonic modes. All values shown in Table 3.1 are approximate, as they were determined by the naked eye from the plots similar to top panel of Figure 3.7. The onset of the amplitude saturation was considered to correspond to critical power.

Table 3.1: Critical heat powers for given temperatures and longitudinal harmonic modes.

Harmonic mode	**Temperature [K]**	$\dot{q}_{crit}$ **[mW]**
First	1.45	55
	1.65	85
	1.83	115
Second	1.45	120
	1.65	195
	1.83	-
Third	1.45	175
	1.65	-
	1.83	-

We have also analysed the power evolution of the corresponding vortex line density measured in the centre of the channel by the attenuation of the transversal second sound mode. The values of the vortex line densities were calculated using equation 1.31 presented in the first chapter. For the calculations we have used the out-of-resonance value (taken as an average of the amplitude values from the beginning and from the end of the measured frequency sweep, see Figure 3.6) of the transversal second sound signal as an unattenuated amplitude. The attenuated amplitude was chosen as a minimum of the transversal signal. The width (FWHM) and resonant frequency of the unattenuated peak were determined from the full transversal frequency sweep which was measured before any turbulence was generated. The mutual friction coefficient B for a given temperature was taken from tabulated values [20]. The calculated vortex line densities have an uncertainty of 30% due to the unrealistic (in this case, at least) assumption of a fully random vortex tangle used in the derivation of equation 1.31

As a result, in Figure 3.7 we show the direct comparison of the longitudinal second sound amplitude and the vortex line density measured in the centre of the channel for the whole range of applied heat powers. We expect different behaviour

of the measured vortex line density for the different harmonic modes due to their different geometrical structure displayed in Figure 3.2. The vortex line density development perfectly fits with the longitudinal peak amplitude evolution for the first harmonic mode. Critical power, for which the longitudinal signal transitions into the turbulent regime (marked by the dotted line) exactly matches the shoot-up of L in the centre of the channel. We have also shown that for the second harmonic mode of the longitudinal signal, which has a node in the scanned area, no significant rise in the amount of quantized vortices was observed during the transition. It strongly implies that the generation of quantized vortices by a standing wave of second sound is localised in the anti-nodes of the temperature wave created.

Unfortunately, we were not able to confirm this hypothesis for the third harmonic mode due to the limitations of the power supply. We were able to observe the turbulent transition for this mode only for the lowest attained temperature 1.45 K (the resulting counterflow velocity for the given power is lower at higher temperatures) and even here, it was on the edge of the power limit. The monotonous increase of the measured vortex line density for all harmonics with the power is caused by parasitic DC counterflow present in the channel. It is caused by the driving mechanism, where the heat power supplied by the AC voltage generator has both a DC and AC component. The steady state value of the vortex line density for the DC counterflow scales as $L \propto V_{cf}^2$ [18], which is in perfect agreement with the observed dependence (as the heat power P is linearly proportional to DC counterflow velocity).

3.4 Turbulence decay

Another essential part of the characterisation of turbulence is the classification of the features in its temporal decay. We studied the time evolution of the vortex line density right from immediately after turbulence generation was stopped. Decays were measured at three different temperatures, 1.45 K, 1.65 K and 1.83 K and for different powers used to generate the initial steady state turbulence. A single decay measurement was executed as illustrated in Figure 3.8. The chosen transversal second sound peak was held on the resonant frequency during whole measurement. The longitudinal signal was driven by the resistive heater at a certain heat power. The corrections on transversal peak shifting due to the overheating of the experimental volume in case of higher power inserted, which were mentioned above were also used here and will be explained in detail later in Section 4.1. At the beginning of the measurement, no power was applied to the channel heater, in order to determine the unattenuated amplitude. After 10 s, the power to the heater was turned on, resulting in vortex generation in the channel and therefore, attenuation of the transversal signal. The turbulence was driven for 30 s to ensure the turbulence was in the the steady state. By switching off the heater, we have initiated turbulent decay from the initial vortex line density. Recovery of the transversal signal amplitude was then measured for at least 60 s until only the remnant vorticity remained. Instead of switching off the heater power completely, we actually redirected (with the use of a relay) the power to the compensation heater (similar to driving heater, but placed in helium bath outside the experimental cell) to maintain the power input to the experiment as

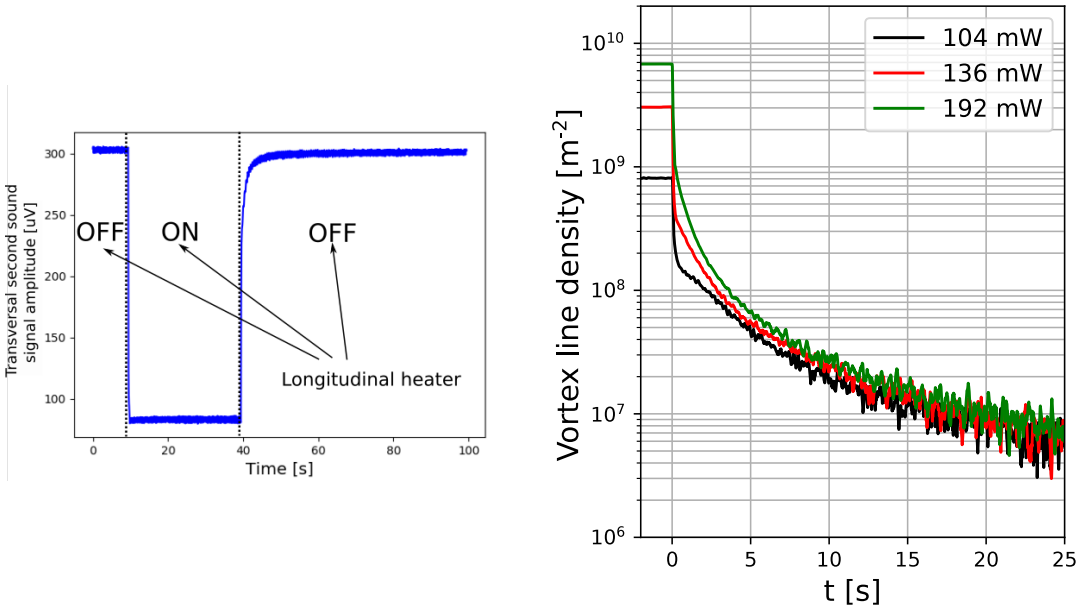

Figure 3.8: Left: Example of a single decay measurement. The transversal signal was held on resonance during the whole measurement. A certain power input into the longitudinal heater was sequentially turned off/on/off. The temporal decay of the turbulence created was measured by monitoring the recovery of the transversal amplitude. Right: Sample decays of the vortex line density for three different initial steady state values.

a whole. Temperature stabilisation would not be possible otherwise.

In all cases, at least 50 single decay measurements were performed to create a single decay plot. All measured transversal attenuation curves were at first averaged for noise suppression. The second sound signal between the capacitative sensors was measured with the phase sensitive Lock-in amplifier, with a 10 ms time constant and 10 ms sampling (wait time). The time evolution of the vortex line density was than calculated with the use of equation 1.31 after the raw data were averaged. The unattenuated amplitude was taken from the beginning of each single decay measurement as an average of the first 30 samples. The width of unattenuated peak was determined from the full transversal frequency sweep measured in advance. The time axis was shifted so that the start of the decay would correspond to $t = 0$ for all single attenuation curves. A sample decay plot created after such processing for three different initial values of steady state vortex line densities is displayed in Figure 3.8.

3.4.1 Decay time scaling

We analysed the time scaling of the measured decays and discovered the existence of two different scaling regimes. The first regime holds just for very short decay times. We refer to it as the early time regime. The majority of the vortex line density vanishes during this part of the decay. Figure 3.9 shows the first two seconds of turbulent decay at 1.65 K of the first harmonics for three different initial vortex line densities. The fast initial decay regime scales with time

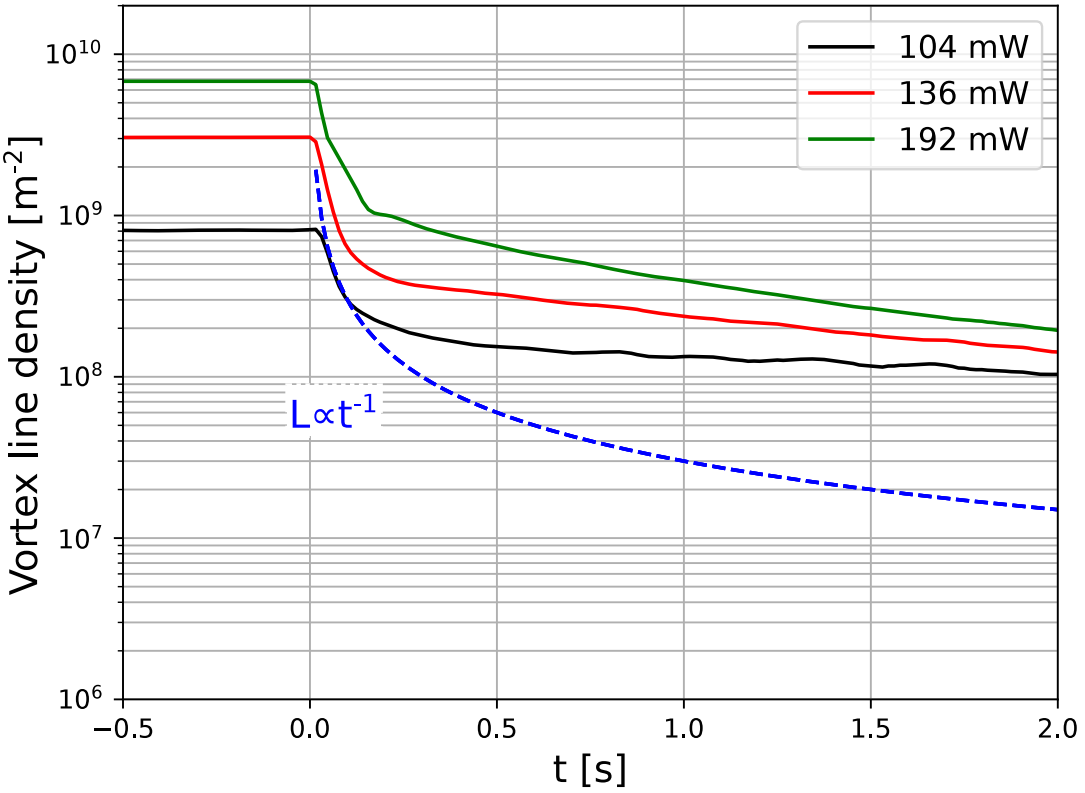

Figure 3.9: Early time decay regime at 1.65 K generated by the first harmonic mode for three different initial vortex line densities. The blue dashed line displays the $L \propto t^{-1}$ scaling law predicted by the Vinen's equation 1.24. The decay clearly follows the dashed line for times of the order of hundreds of milliseconds. After that, it deviates from this scaling regime and the decay slows down.

as $L \propto t^{-1}$ for times of the order of hundreds of milliseconds. Then the decay curve deviates from this scaling law and continues to the transition regime where the decay slows down. The observed scaling law indicates Vinen-like decay via the annihilation of oppositely oriented vortex segments in a completely random tangle. Such turbulence was described in the first chapter in section 1.3.2.

The initial Vinen-like decay then transforms into another scaling regime. We designate this, the late time regime. Figure 3.10 displays the decay measurements from 2 s until their end. Both horizontal and vertical axis are modified by the values of the virtual time origin t_0 and the remnant vortex line density L_r. Values of these parameters were obtained from the fit applied to the time range spanning 5 s to the end of studied decay. The fitting function used has the form of equation 1.22 with fitting parameters L_0, t_0 and L_r:

$$L(t) = \frac{L_0}{(t + t_0)^{-\frac{3}{2}}} + L_r. \tag{3.1}$$

The resulting plot clearly shows that the observed decays obey the $L \propto t^{-\frac{3}{2}}$ scaling law of Kolmogorov-like turbulence. This scaling holds from couple of seconds after the decay's start until the end of the decay process. We can then

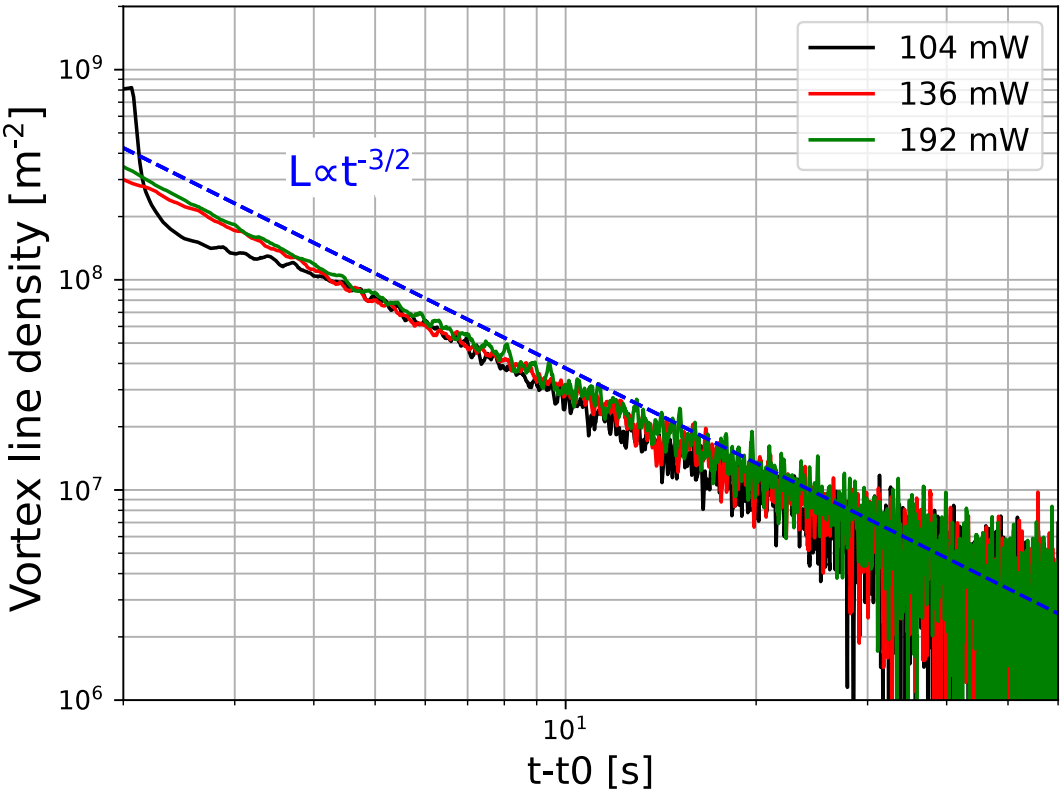

Figure 3.10: Late time decay regime at 1.65 K for three different initial vortex line densities. Horizontal and vertical axes are shifted by the values of the virtual time origin t_0 and the remnant vortex line density L_r. The dashed blue line displays the $L \propto t^{-\frac{3}{2}}$ scaling.

conclude that the turbulent decay has a quasi-classical form in the time domain discussed with a cascade-like energy transition from large scales to the smallest, where it is eventually dissipated (either due to viscous dissipation in the normal component via mutual friction or via the continuation of the cascade towards the formation of Kelvin waves on the quantized vortices). Such decay behaviour is typical, e.g., for coflow turbulence past a grid [12], but has been observed in other types of experiments in superfluid ^{4}He and ^{3}He.

3.4.2 Temperature and initial vortex line density dependence

At each measured temperature, we performed decay measurements for different values of heat power. This resulted in steady state turbulence with different initial vortex line densities from which the decay started. We always used the maximum possible power for one of the decays. Another value of heating power was chosen to be just above the critical value. A direct comparison between decays with different initial vortex line densities generated by the first harmonic mode at 1.45 K is displayed Figure 3.11.

We can describe the initial vortex line density dependence of the decay con-

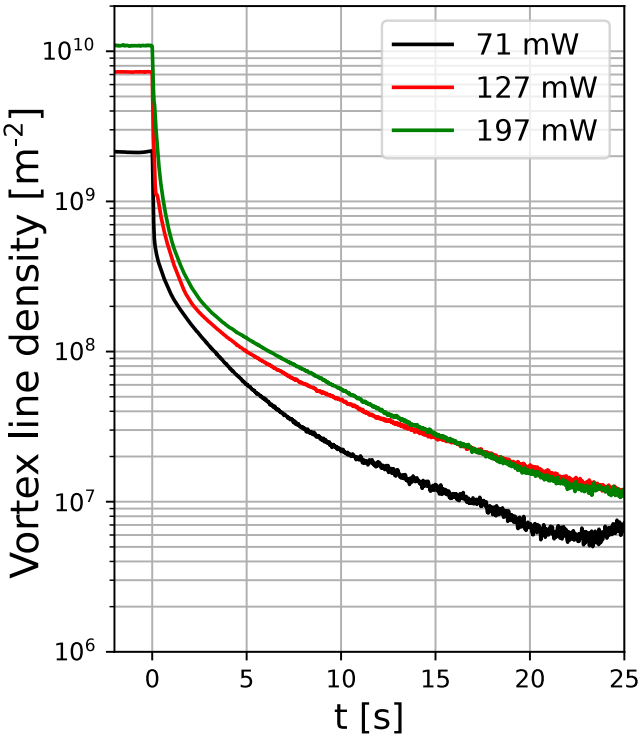

Figure 3.11: Measured decays at 1.45 K for three different initial values of vortex line density of steady state turbulence generated by the first harmonic mode. The green line represents the decay of the maximum vortex line density achievable. Two different turbulent regimes are visible, where the decay curves starting from higher initial values of L tend to collapse, displaying universal behaviour at late times, unlike the low starting density curve.

sidering the data in Figure 3.11. Here at 1.45 K, we have observed different decay behaviour with different initial L. The decay curves starting from higher initial values of L tend to collapse to universal behaviour for the late time decay regime. However, it is not true for the decay of quantum turbulence, which is initially driven with heating powers just above the critical value. The difference between the two observed turbulent regimes may be connected either with the respective amounts of quantized vorticity generated by the second sound standing wave and by DC counterflow, or with different states of the normal component in such turbulent flows. For a full understanding of this phenomenon, further analysis is needed which is beyond the scope of this thesis.

Next, we show the temperature dependence of the decays studied, with use of the first longitudinal harmonic mode. Figure 3.12 shows the decays measured at three different temperatures. For each temperature, three decays starting from different initial vortex line densities were measured. The decays show different behaviour of the transition regime between the early time decay (Vinen-like) and the late time decay (Kolmogorov-like) with varying temperature. Specifically, the appearance of a partial slowdown of the decay in the transition regime be-

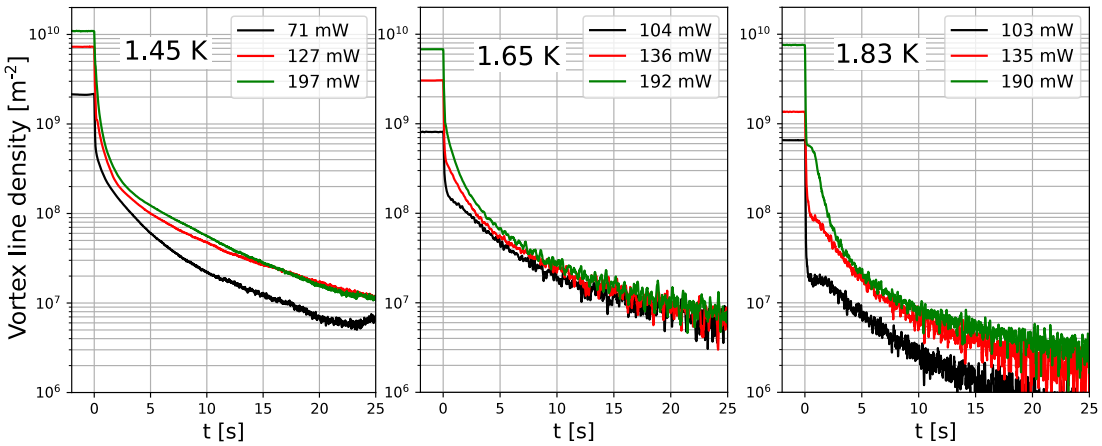

Figure 3.12: Temperature dependence of decays at 1.45 K, 1.65 K and 1.83 K for various steady state vortex line densities. Differing behaviour of the transition between the early time decay and the late time decay was observed. A partial slowdown of the decay becomes more significant with increasing temperature, resulting in the "bump" for the highest temperature, which is a characteristic feature of DC counterflow (see text).

comes more significant with increasing temperature. In some cases at the highest temperature, a temporary increase of the vortex line density during the decay may even be spotted. This local maximum, or "bump", is characteristic of DC counterflow as described in [24]. A theoretical explanation for the occurrence of the so-called bump in DC counterflow may be found in [25].

4. Discussion

4.1 Temperature shifting of second sound resonances

We have already stated that the resonant frequencies of the second sound peaks shift with changes of temperature due to the variation of the second sound velocity. This can affect temporal measurements of the second sound amplitude at a fixed frequency. Such measurements have been performed in our experiment to determine the vortex line density by the attenuation of the transversal second sound signal in both turbulent steady state and decay measurements. In cases of high power input into the experiment, overheating of the experimental volume visibly occurred. This is confirmed by the frequency shifts of the transversal peaks measured for different longitudinal heater powers, which are displayed for 1.45 K measurements in Figure 1.8 in the first chapter. The reason for the occurrence of overheating is that the experimental volume is closed (besides the small leaks around the brass holders and around the capacitative sensor's frames), meaning the thermal connection with the helium bath is weak. However, the shifting of the second sound peaks was also observed in experiments with thermal counterflow in a partially open channel, as discussed in [26]. But the observed shifts for similar heat powers were significantly lower.

The actual amplitude of a second sound peak measured at fixed frequency near the resonance may be reconstructed when values of both complex amplitude components (absorption and dispersion signals) are available [26]. When considering the plane of the complex amplitude, we obtain a circular shape for the full resonant peak. By plotting a series of the transversal second sound peaks with various different attenuation levels, as shown in Figure 4.1 (left), we will obtain a set of (distorted) circles, as shown in Figure 4.1 (right). The displayed circles tend to collapse to one point (defining the values of the complex amplitude components for the resonant signal background) for the signal position far from the resonance. Here, the background value is independent of the attenuation level, and also the actual position of the resonance. A single measurement of the transversal signal's complex amplitude at a frequency close to the resonance, then represents one point in the discussed space (blue diamond in Figure 4.1 (right)) and may be associated to a resonance with a certain amplitude. By suitable interpolation, the whole complex plane may be converted into a real amplitude value mesh. This way, the real amplitude of the transversal second sound peak may be determined, as long as the measurement is not done too far from the resonance. The resolution of this technique decreases as the measured frequency deviates from the true resonance and may be considered appropriate if the deviation does not exceed the width of the peak (FWHM).

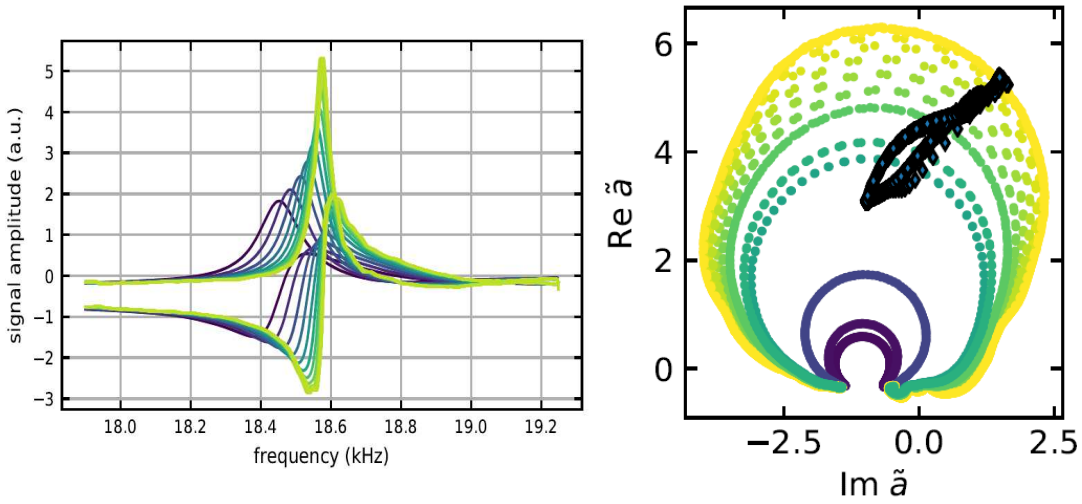

Figure 4.1: Left: Series of transversal second sound peaks measured at different attenuation levels (increasing vortex line density) in the thermal counterflow experiment [26] at 1.95 K. The frequency shifting of the resonances due to overheating is clearly visible. Right: The same transversal second sound peaks measured for different attenuation levels displayed in the plane of the complex amplitude $\tilde{a}$. The colour of single peaks indicates the corresponding real amplitude (from bright yellow for the unattenuated signal to dark blue for the most attenuated peak). The second sound signal measurement at fixed frequency (close to resonance) with time-dependent attenuation is displayed as a series of blue diamonds.

4.2 DC counterflow influence

The longitudinal second sound signal used in our experiment for the generation of quantum turbulence was driven by a function generator supplying a resistive heater. The voltage signal on the heater has the form of a harmonic wave function $U_0 cos(\omega t)$ with U_0 being the signal amplitude. The actual time-dependent heat power on the heater, given as U^2/R, is then:

$$P = P_{DC} + P_{AC} cos(2\omega t) = \frac{U_0^2}{2R} + \frac{U_0^2}{2R} cos(2\omega t), \tag{4.1}$$

resulting in both AC and DC components in the power signal. The AC component of the resulting power was used for the generation of a second sound standing wave, i.e., the oscillatory counterflow with a frequency double that supplied by the generator. The second (DC) component of the heat power establishes a thermal counterflow, with counterflow velocity $v_{ns,dc}$ (or V_{cf}) given by equation 1.23. However, the exact geometry of such a counterflow is unknown, since the channel is closed. Small leaks around the brass holders (used to position the heater and thermometer) and around the capacitative second sound sensors may have lead to jet-like counterflows into the channel.

We have already shown in the inset of Figure 3.7 that the observed background of the steady state vortex line density scales similarly to thermal DC counterflow as $L \propto V_{cf}^2$. At 1.45 K, we obtained the V_{cf} dependence of the vortex line density seen for the second longitudinal harmonic mode. All the turbulence measured for this mode should therefore be generated by the DC counterflow, as we scan the

area around a node of the resonant standing wave. The counterflow velocity was calculated from the heat power via equation 1.23 with values of the temperature dependent helium properties taken from [22]. This was done in order to determine the critical values for vortex generation in the observed DC counterflow and for comparison with previous results. A similar analysis as was used in Ref. [18], was applied to our data . The dataset of the measured vortex line densities L and calculated counterflow velocities V_{cf} was fitted with a function in the form:

$$L = L_0 + A(V_{cf} - V_{cf,crit})^2. \tag{4.2}$$

The obtained value of the parameter $L_0 \approx 7 \times 10^7\,\mathrm{m}^{-2}$ should describe the amount of remnant vortices. The prefactor A contains information on the effective kinematic viscosity of turbulent He II, which is beyond the scope of this work. Finally, we found the value of the critical velocity for the observed DC counterflow (which occurs before the oscillatory counterflow sets in) to be $V_{cf,crit} \approx 0.26\,\mathrm{cm/s}$. As a comparison with the results from Ref. [18], the observed values of L_0 was of the order of $10^6\,\mathrm{m}^{-2}$ and $V_{cf,crit} \approx 0.2\,\mathrm{cm/s}$ for quantum turbulence generated by thermal counterflow in a channel of the same lateral dimensions. The critical velocity for DC counterflow in our experiment is therefore in good agreement with previous studies.

To better illustrate the steady state behaviour of quantum turbulence generated by the oscillatory counterflow, we have subtracted the L_{2harm} values observed for the second longitudinal harmonic mode (as it contains the DC background) from the L_{1harm} values for the first mode. As a result, it should only display the contribution of the oscillatory counterflow to the generation of quantum turbulence. The difference of two inferred vortex line densities is shown in Figure 4.2 against the values of heat power. The displayed heat power axis is shifted by the value of the critical power, $P_{crit} = 50\,\mathrm{mW}$, determined from the onset of increased vortex line density. The relation of heater power to oscillating counterflow velocity will be discussed in more detail, later.

In Figures 4.2 and 3.7, we observe two different regimes of steady state turbulence generated in oscillatory counterflow. The first sets in at the critical heat power for the generation of quantized vortices, with a fast increase of vortex line density showing power law scaling with an exponent of ~ 2.5, which then transits to a slower regime. In the second regime, we have observed a scaling of the vortex line density (originating from oscillatory counterflow) with supercritical heat power according to a power law with an exponent of ~ 1.3. Unfortunately, we can not say more on the scaling. Further investigation of the observed steady state regimes would bring interesting information on this newly studied type of quantum turbulence. However, further analysis from more measurements would be needed. Also, a more exact characterisation of the geometry and the influence, or suppression, of the DC counterflow in this experiment is necessary.

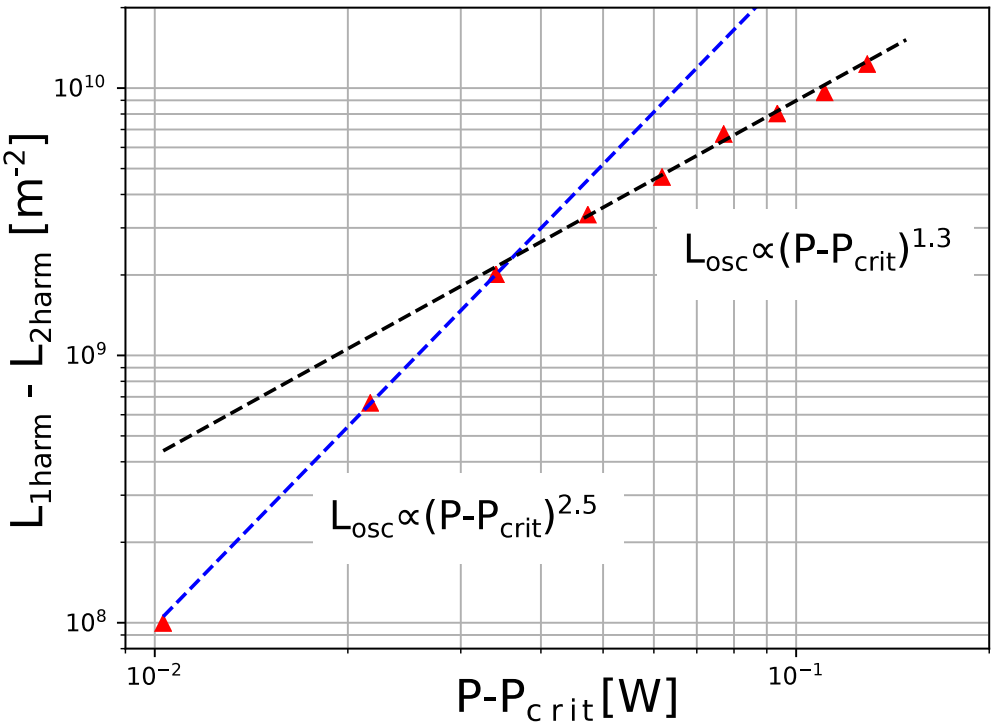

Figure 4.2: The contribution of oscillatory counterflow to the vortex line density measured at 1.45 K. On the vertical axis, we show the difference of vortex line density measured for the first and second longitudinal harmonic mode, corresponding to the contribution of oscillatory counterflow. The horizontal axis displays heat power, which is shifted by the critical power, determined from the point L rapidly increases. The dashed lines represent the power law fits of the two observed regimes. We note that the vortex line density from DC counterflow corresponds to $L_{2harm} = 2 \times 10^8\,\mathrm{m}^{-2}$ at the critical power and remains approximately an order of magnitude below the vortex line density during the second regime above $P - P_{crit} = 40$ mW, c.f. Figure 3.7.

4.3 On the velocity amplitude of the oscillatory counterflow

We have already stated above, that two (DC and AC) counterflow contributions are present, resulting from the voltage signal applied to the heater. We have also described the behaviour of the DC counterflow velocity. The question here is, how to determine the velocity $v_{ns,ac}$ of the oscillatory part of the studied counterflow. We expect $v_{ns,ac}(t) = v^i_{ns,ac}.cos(2\omega t)$, similarly to the AC component of the heater power, with i indexing different ways of estimating the velocity amplitude.

Two different approaches are possible. The first is based on the idea that the counterflow velocity of the oscillatory part is the same as the one given for the DC contribution, but resonantly enhanced by the Q factor of the resonance. This way, we can derive $v^I_{ns,ac}$, based on the equation 1.23 as:

$$v^I_{ns,ac} = \frac{P_{AC} Q}{AST\rho_s} \tag{4.3}$$

with a magnitude of alternating heat power over the area A. In our experiment, the observed quality factors for the longitudinal resonances were of the order of 10. But, this approach to the oscillatory counterflow velocity is valid only in the sub-critical region (below which the critical velocity is reached) of Lorentzian resonances, because above the critical power, $v_{ns,ac}$ will be suppressed in the anti-nodes in the same manner as shown for the thermometer voltage signal in the previous section. Moreover, there is no straightforward manner in which to define the Q factor for non-Lorentzian resonances.

Another window to determining the velocity of the oscillatory part of the counterflow is from the direct measurement of the magnitude of the temperature changes δT observed in the channel. The same approach was used in the work of Kotsubo and Swift [23], assuming a harmonic time dependence and spatial profile of the resonant standing wave. Following the same reasoning that equation (13) was obtained in Ref. [23], we can find the oscillatory counterflow velocity.

$$v_{ns,ac}^{II} = -\frac{\rho S}{u_2 \rho_n} \delta T. \tag{4.4}$$

Here, ρ represents the total density of He II, S the specific entropy, ρ_n the density of the normal component and u_2 is the second sound velocity. The values of δT may be determined from the voltage signal measured on the resistive thermometer, which was biased by a constant current of 1 μA, as long as a resistance-temperature calibration is available. The temperature derivative of the voltage is then proportional to the temperature derivative of resistance, multiplied by the current, $dU/dT = I.dR/dT$ and can be used to calculate the temperature oscillation amplitude as $\delta T = \sqrt{2}U/(dU/dT)$. The prefactor $\sqrt{2}$ is necessary to convert the acquired RMS (Root-Mean-Square) voltage signal (shown in the top of Figure 3.7) to a voltage amplitude. The velocity determined in this manner should hold for the whole region of heat powers unlike $v_{ns,ac}^{I}$, as it is taken from experimentally observed quantities.

In Figure 4.3, show the comparison between values of $v_{ns,ac}^{I}$ and $v_{ns,ac}^{II}$ as functions of the heat power. It was done for all three longitudinal harmonic mode measurements at 1.45 K (similar behaviour is observed at the other temperatures). We expect common behaviour of both velocities in the sub-critical region, and then a deviation of $v_{ns,ac}^{I}$ from realistic behaviour. But, this is true only for the first harmonic mode. For both the second and the third harmonic, the calculations of $v_{ns,ac}^{II}$ are strongly undervalued in the sub-critical regime. The real oscillatory counterflow velocity for a given heat power is expected to be between two limiting cases given by $v_{ns,ac}^{I}$ and $v_{ns,ac}^{II}$, but we do not possess enough information for a more accurate determination.

We can only hypothesize as to the possible reasons of the deviation in behaviour between the presented velocities for the higher resonant modes. Either the assumption of the harmonic profile of the heat wave used for the derivation of $v_{ns,ac}^{II}$ is incorrect, which should affect all of the harmonic modes, or we get incorrect readings from the thermometer. There may indeed be issues with its thermalization, since the observed frequency dependence of the deviation of $v_{ns,ac}^{II}$ seems to favour this option. Furthermore, additional systematic phase shifting seen in the longitudinal spectrum (Figure 3.3) for higher harmonic modes, with values of ~ 20 degrees for the second and ~ 40 degrees for the third harmonic was

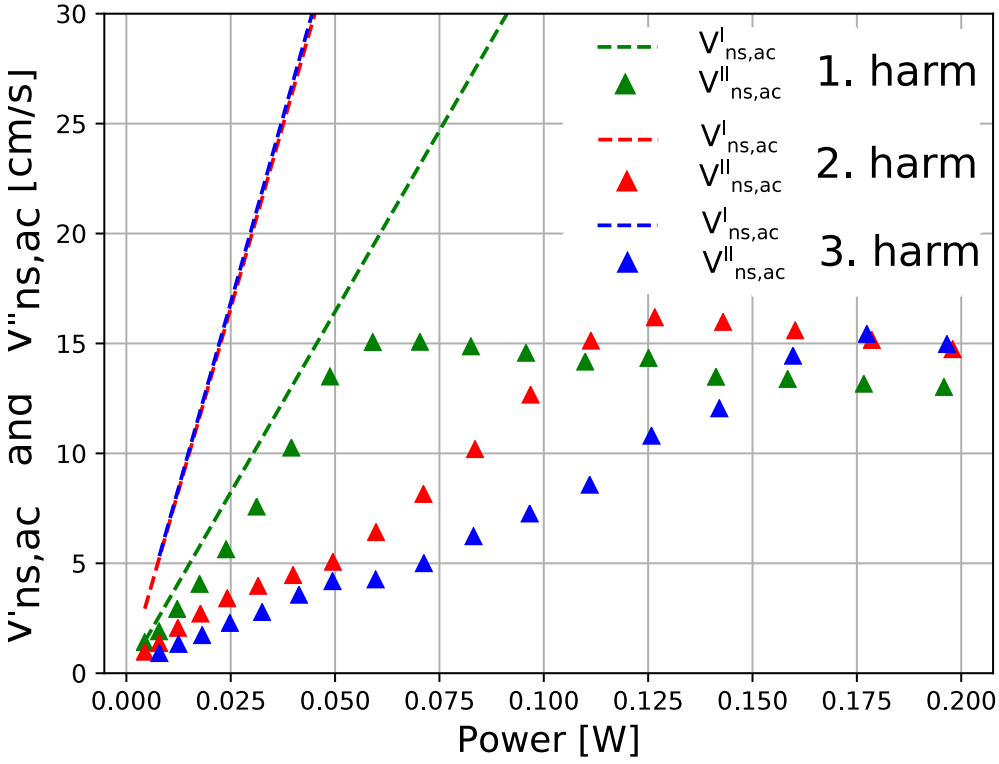

Figure 4.3: Values of oscillatory counterflow velocity determined by two different approaches as a function of heat power at 1.45 K. Dashed lines represent $v^I_{ns,ac}$, for the three observed harmonic modes, which were determined via the equation 4.3 as resonantly enhanced velocities. This approach is expected to be valid only for sub-critical velocities. The triangles show the values of $v^{II}_{ns,ac}$ obtained from direct measurements of the magnitude of temperature changes observed in the channel, given by the equation 4.4. The Q factors obtained for the three lowest longitudinal resonant modes are 10.2, 20.6, and 20.9, in the order of increasing mode number.

determined during single peak analysis. This may also be caused by the effect of imperfect thermalization, but at this point, more evidence would be necessary to prove this explanation.

4.4 Temperature dependence of critical velocity

The values of the critical parameters for turbulence generation in oscillatory counterflow may be determined from the observed onset of vortex line density seen by the transversal second sound signal in the centre of the channel. This is of course possible, only for the measurements with the first longitudinal resonant mode as no observable onset of an increase of L was seen for higher harmonics. For the second harmonic mode, it was due to its geometrical structure in the channel. For the third harmonic mode, it was caused by the observation of only the sub-critical and transitional oscillatory flow regime.

For the first longitudinal harmonic mode (at all temperatures), we expect the oscillatory velocity $v^I_{ns,ac}$, determined by equation 4.3, to correspond with the

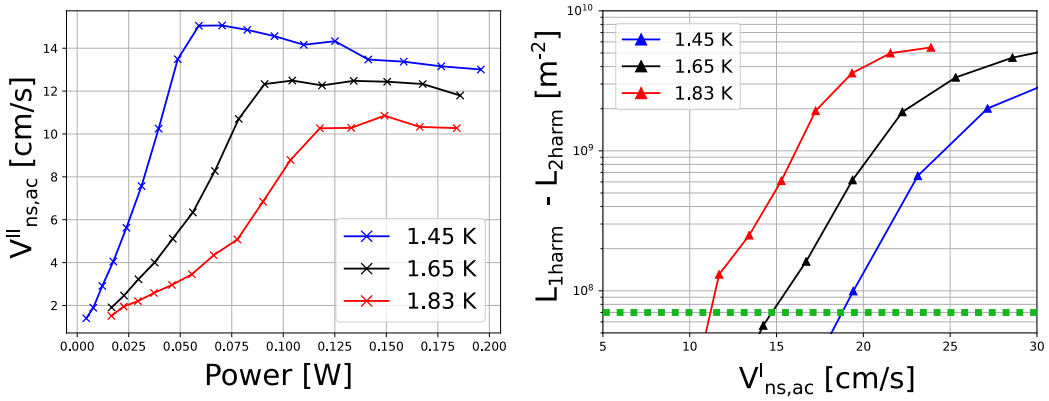

Figure 4.4: Left: Oscillatory counterflow velocity obtained from the amplitudes of longitudinal resonances via equation 4.4 as a function of heat power, for three temperatures. Saturation of $v^{II}_{ns,ac}$ determines the critical value of the displayed velocity. Right: Oscillatory counterflow contribution to L (difference of values observed for first and second mode), as a function of $v^{I}_{ns,ac}$. The rapid increase of vortex line density above the level of remnant vorticity (highlighted by the green dotted line) shows the position of the critical velocity.

real oscillatory flow velocity, as long as the sub-critical region is only considered. Therefore, on the edge of the turbulent transition, it should still be an adequate quantity for the determination of the critical parameter. In the right panel of Figure 4.4, we show the oscillatory counterflow contribution to the vortex line density (the difference of values observed for first and second mode), for different temperatures, as a function of $v^{I}_{ns,ac}$. The critical velocities, when a rapid increase of L starts (above the level of remnant vorticity) are easily seen in the plot and their values for different temperatures are listed in Table 4.1.

Table 4.1: Critical oscillatory counterflow velocities obtained by two different approaches, for all studied temperatures.

Temperature [K]	**critical $v^{I}_{ns,ac}$ [cm/s]**	**critical $v^{II}_{ns,ac}$ [cm/s]**
1.45	18.5	15
1.65	14.5	12.5
1.83	11	10.5

Another approach to determining the critical parameter for the studied oscillatory counterflow is via the directly measured temperature changes in the channel. It leads (see equation 4.4) to the values of $v^{II}_{ns,ac}$, which may also represent the required critical parameter. For this purpose, we plot $v^{II}_{ns,ac}$ obtained from the amplitudes of longitudinal resonances as a function of heat power applied to the channel. This was done for three different temperatures, as may be seen in left panel of Figure 4.4. The saturation of this velocity indicates the occurrence of the turbulent transition (as already stated), therefore the saturated value should

represent the critical oscillatory counterflow velocity. These critical velocities are shown in Table 4.1 for comparison with the ones obtained from the $v^I_{ns,ac}$ velocity analysis.

The results in Table 4.1 show a reasonable agreement of the two different approaches used for the determination of the critical oscillatory counterflow velocity for formation of quantised vortices. The observed temperature dependence of the critical velocity qualitatively corresponds with the conclusion of the previous study by Kotsubo [23].

4.5 Frequency dependence of steady state turbulence

As we are considering the oscillatory flow of He II, we should expect similarities with others, i.e., mechanically driven, oscillatory flows. Here, we concentrate on the frequency dependencies of the critical parameters causing instabilities. For the mechanically driven oscillatory flows of He II, the critical velocity scales as $v_{crit} \propto \sqrt{\kappa\omega}$ [27], where κ represents the circulation quantum. Similar scaling of the critical oscillatory counterflow velocity with $\sqrt{f}$ was observed by Kotsubo and Swift [23].

More detailed studies on oscillatory flows of superfluid helium (He II) may be found in [27] and as well as Ref. [28], on which the author of this thesis collaborated and may be found in the Appendix. The flows discussed are typically observed in the vicinity of various oscillating mechanical resonators such as quartz tuning forks and superconducting vibrating micro-wires driven in magnetic fields, which have also been utilised in studies of ^{3}He flows at very low temperatures [29].

To comment on the frequency dependence of the critical velocity in our experiment, special care on the estimation of the observed critical parameters must be taken. Mainly, the approach used to estimate the oscillatory velocity and how the transition onset is determined must be considered. Above, we discussed that the thermometer's response may be questionable in the case of higher resonant modes. Yet, we do not have information about the inset of turbulence from the transversal signal attenuation measurements (as we used for the temperature dependence determination, where only the first harmonic modes have been used), where no obvious increase of L was spotted for these modes (for reasons already discussed).

The best estimation of the critical oscillatory velocity we have is the value of $v^{II}_{ns,ac}$ for the saturated voltage signal of the longitudinal resonance. As a result, the critical velocity in the oscillatory part of the counterflow seems to be frequency-independent with a value of $\sim$ 15 cm/s (at 1.45 K), as shown in Figure 4.3. The disagreement with Kotsubo's frequency scaling may be caused by two effects: Either our estimation of the critical velocity for the higher harmonic modes are incorrect due to insufficient thermalization time for the thermometer, as discussed above, or that we may be observing a different transition than the one seen in the previous study. As the quality factors of the resonances used by Kotsubo and Swift were significantly higher (100 - 1000, probably caused by the different geometry and material of his channel) in their case, the first instability occurred in the strongly enhanced oscillatory contribution of the studied coun-

terflow. We have shown that in our case, the instability in the DC component sets in first and is already present before reaching the critical parameters for the oscillatory flow. Therefore, we are observing the transition between two different types of turbulent flow, which would probably lead to different frequency scaling.

4.6 Comparison to previously studied channel flows in He II

First, we are to comment on previous experiments on steady state quantum turbulence in channel flows [18, 30, 31]. Different behaviour was found for coflow in contrast to counterflow and superflow. The presented flows differ in both scaling of vortex line density with flow velocity and their temperature dependence. For coflow, temperature independent scaling $L \propto V_{cf}^{3/2}$ was found, unlike for counterflow and superflow with scaling $L \propto V_{cf}^{2}$ along with strong temperature dependence [18]. The similarity of counterflow and superflow is based on the idea that superflow is just counterflow in the normal fluid's frame of reference.

From the analysis applied to our data on oscillatory counterflow, we can not directly comment on the vortex line density scaling with oscillatory counterflow velocity. However, we have found two different scaling regimes in terms of supercritical heat power dependencies in the steady state of quantum turbulence in oscillatory flow, as seen in Figure 4.2. Right above the critical power (rather high in comparison to previously observed flows), a rapid increase of L is seen with a power law scaling with an exponent of ~ 2.5. Later, a different scaling sets in with a rather smaller slope of ~ 1.3. The temperature dependence of the vortex line density behaves with the same trend as counterflow and superflow [18], as may be seen in the right panel of Figure 4.4. But unlike for these flows, we have also found the temperature dependence of the critical velocity, as was also found in the experiment of Kotsubo [23].

Differences between coflow on one side, and superflow or counterflow on the other have also been observed in turbulence decay [12, 24, 31]. For coflow, the universal scaling law of $L \propto t^{-3/2}$ occurring within a few seconds after the decay's start was found, holding to the very end of the decay (the order of minutes). Derivation of this scaling is built on the presence of a quasi-classical cascade-like transfer of energy from large to small scales with a Kolmogorov-like energy spectrum. Both counterflow and superflow show the same universal scaling in the late time decay regime. In the short times after the start of the decay, different scaling has been observed with a fast drop in the vortex line density, $L \propto t^{-1}$ for these flows. Such scaling may be found from the decay term of Vinen's equation 1.24 describing the decay of a completely random vortex tangle via the mutual annihilation of oppositely oriented segments. However, the behaviour of decays observed strongly differs for the transient regime between the two mentioned scaling laws. It is in the form of a local maximum, or the so-called "bump", occurring in counterflow, which is not always true for superflow [24].

We have already shown in Figures 3.9 and 3.10 the presence of both scaling regimes in the studied oscillatory counterflow, similar to counterflow and superflow. In Figure 4.5, we show the direct comparison of decays for the oscillatory counterflow, the DC counterflow and the superflow in the channel with the same

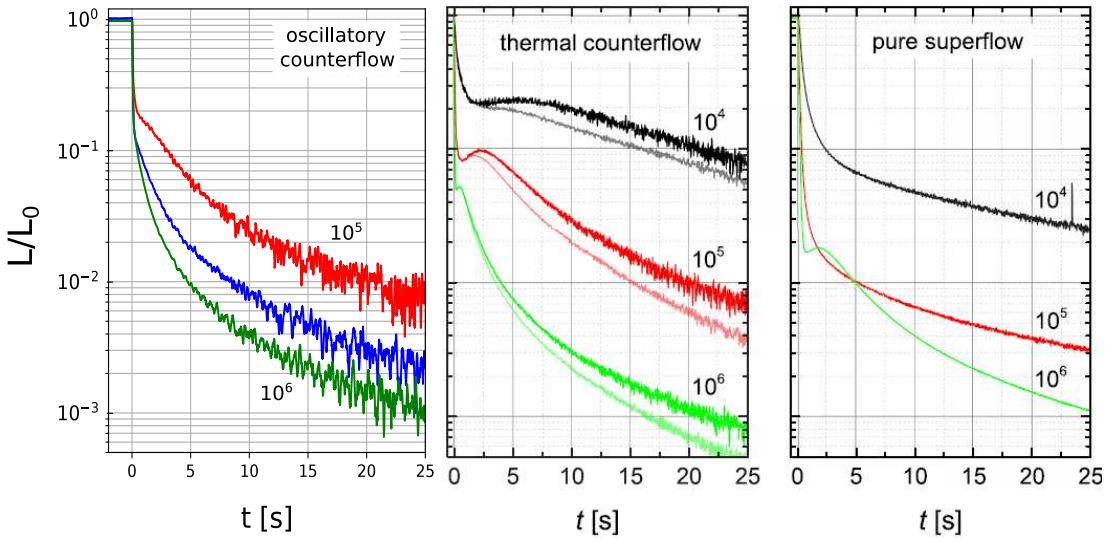

Figure 4.5: Direct comparison of decays for oscillatory counterflow (left), DC counterflow (middle) and superflow (right). All flows were studied in a channel with the same cross-section (1×1 cm) at the same temperature (1.65 K). The initial steady state densities for the decays are $10^4, 10^5$ and $10^6 \mathrm{cm}^{-2}$. The vertical axis displays values of L relative to the initial vortex line density L_0.

cross-section (1×1 cm), at the same temperature (1.65 K) and from similar initial values of the steady state turbulence. The results on DC counterflow and pure superflow may be found in [24].

The behaviour of the transient regime of turbulent decay in oscillatory counterflow was found to be different from both DC counterflow and pure superflow. At the temperature shown here (Figure 4.5), no evident bump-like increase of L is revealed, as it is always for DC counterflow and the highest initial vortex line density measurement for superflow. This feature of turbulent decay was seen in our experiment only at the highest investigated temperature (1.83 K), which was shown in the right panel of Figure 3.12. Furthermore, the "bump" observed at 1.83 K behaves similarly to the one typically occurring in DC counterflow, while it gets broader for smaller initial L values. But still, we need to bear in mind that not only oscillatory counterflow, but also DC counterflow, are involved in our experiment, which may influence the results. For more precise characterization of turbulent decay in the pure oscillatory counterflow, an experiment where the DC counterflow is completely suppressed would have to be devised.

Finally, we have analysed the time ranges for which the initial $L \propto t^{-1}$ scaling of decay holds in quantum turbulence generated by oscillatory counterflow, as was done for DC counterflow and superflow in [24]. The results are shown in Figure 4.6. We can conclude that in the case of oscillatory counterflow, the decay obeying Vinen's prediction holds for the shortest time, from all displayed flows, which is in the order of tens of milliseconds. The qualitative behaviour of decays from different initial vortex line densities is the same for all types of flow, as $L \propto t^{-1}$ scaling is always followed longer for the decays starting from lower initial L.

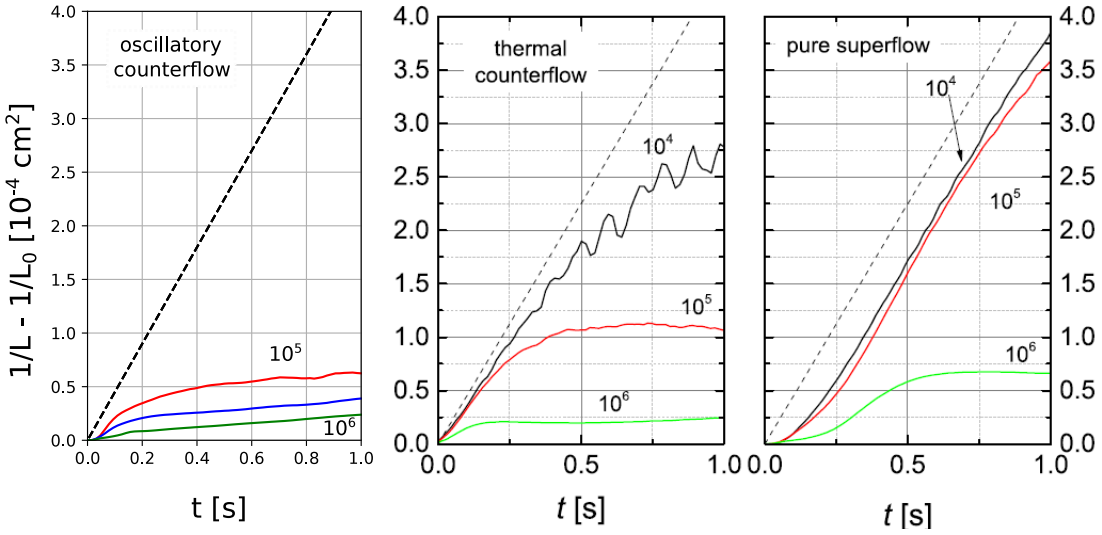

Figure 4.6: Comparison of the ranges of validity of the initial $L \propto t^{-1}$ scaling in oscillatory counterflow (left), DC counterflow (middle) and superflow (right). All plotted decays have been measured at 1.65 K. The black dotted line displays the theoretical prediction for the early time decay given by Vinen's equation 1.24. Results for DC counterflow and pure superflow are taken from Ref. [24].

Conclusion

We have presented results of our study on quantum turbulence generated by oscillatory counterflow. Turbulence was generated by the so-called longitudinal standing wave of second sound, which was driven by a resistive heater supplied with an alternating voltage. To detect this wave, we used a resistive thermometer biased with a constant current. We used another second sound signal (the so-called transversal signal), perpendicular to the longitudinal one, to infer the vortex line density generated by the second sound attenuation technique. These measurements were performed for the first three longitudinal second sound harmonic modes at three different temperatures, 1.45 K, 1.65 K and 1.83 K. Analysis of the data collected lead us to these conclusions:

- First, we confirmed the ability of second sound to generate quantum turbulence, by repeating the experiment of Kotsubo and Swift [23]. By varying the driving heat power, we have found two distinct regimes, for the harmonic modes utilised: The laminar regime where Lorentzian resonant peaks were observed. And the turbulent regime which is characterised by the saturation of peak's amplitude. The critical heat power was found to increase with both temperature and harmonic number.

- We observed attenuation of the simultaneously measured low amplitude transversal second sound, allowing us to directly infer a vortex line density L created in the centre of the channel, undeniably proving that the longitudinal second sound generated quantized vortices. Further, we proved that the generation of vortices was localised to the anti-nodes of the standing wave via measurements of L for the various harmonic modes. No additional vortex line density was seen for the second harmonic mode, despite the saturation of the longitudinal resonance.

- In our experiment, two counterflow contributions (a DC and an AC one) were present, due to the voltage applied to the heater. We showed that the background vortex line density, seen for the second harmonic mode, originates from the DC counterflow, and scales with the DC counterflow velocity as $L \propto V_{cf}^2$, in agreement with Ref. [18]. By subtracting the DC contribution from the measured L, we found two different scaling laws for oscillatory counterflow with supercritical heat power. In the first regime with a fast increase of L, we observed power law scaling with an exponent of ~ 2.5, which then transits to scaling with an exponent of ~ 1.3.

- We have presented two different approaches to determine the oscillatory counterflow velocity. One was based on the theoretical prediction of the resonant enhancement of DC counterflow velocity by the quality factor of the resonance. We argued that validity of this approach is restricted to sub-critical velocities. The other velocity estimation method was based on real measurements of the temperature change in the channel, similar to that used by Kotsubo and Swift [23].

- We observed the temperature dependence of the critical velocity in oscillating counterflow, and found it to be in agreement with [23]. We also

found similar temperature dependence of the measured vortex line density as Ref. [18]. However, no frequency dependence was found for the critical velocity, contrary to expectations. This may be because we actually observed a different form of turbulent transition, as the DC counterflow is already turbulent when the instability occurs in the oscillating counterflow.

We have also characterized the of the decay quantum turbulence generated by second sound. Our finding can be may be summarized as the following:

- Two time scaling decay regimes were found which correspond to previous observations of the decay of DC counterflow and superflow [18, 24] generated turbulence. At early times, Vinen-type decay of the vortex line density, $L \propto t^{-1}$ was found. This regime held for times of order of tens of milliseconds after the decay initiation (which is shorter than in DC counterflow and superflow). In the second, late time regime, Kolmogorov-type ($L \propto t^{-\frac{3}{2}}$) decay was seen, and continued until the end of the decay.

- The differences in the behaviour of the decay for various initial vortex line density values revealed the existence of two regimes. These regimes are most probably caused by different hydrodynamical states of the normal fluid component or by different weighting of DC counterflow contribution. The observed behaviour also differ with changes of temperature, which affect the transition between the early and late time decay regimes. The occurrence of a temporary increase in the vortex line density, known as the "bump", which is typically observed in the decay of DC counterflow generated turbulence and for high initial vortex line densities in superflow [24], was seen only at the highest investigated temperature (1.83 K).

Finally, we would like to comment on the future perspectives of the studies discussed here. Further development of the channel geometry to obtain higher quality factors for longitudinal resonances would help to suppress the contribution of the DC counterflow, as lower critical powers for oscillatory counterflow should be achieved. Further studies of the transversal spatial homogeneity of the vortex tangle created in the steady state are also possible with the use of different low harmonic modes of transversal second sound resonances for vortex detection as is discussed in Ref. [18]. Finally, the use of multiple different longitudinal second sound harmonic modes for the initial generation of vorticity may reveal more information on the decay behaviour of the type of quantum turbulence in question. However, the experimental geometry must be reconsidered due to the localized structure of the turbulence generated.

Bibliography

[1] L.D. Landau, and E. M. Lifshitz, *Fluid Mechanics*. Second English Edition. Pergamon Press, (1987). ISBN 0-08-033932-8.

[2] V. Uruba, *Turbulence*. ČVUT v Praze, Fakulta strojní, (2009).

[3] S. B. Pope, *Turbulent Flows*. Cambridge University Press, (2000). ISBN 9780511840531.

[4] V. F. Sears, E. C. Svensson, P. Martel, and A. D. B. Woods, *Neutron-scattering determination of the momentum distribution and the condensate fraction in liquid* ^{4}*He*. Phys. Rev. Lett., **49**(4): 279-282, (1982).

[5] E. L. Andronikashvili, Fiz. Zh. **10**, 201 (1946).

[6] L. Skrbek a kol., *Fyzika Nízkých Teplot*. Matfyzpress, (2011). ISBN 978-80-7378-168-2.

[7] C. F. Barenghi, R. J. Donnelly, W.F. Vinen (Eds.), *Quantized Vortex Dynamics and Superfluid Turbulence*. Springer, (2001). ISBN 978-3-540-45542-4.

[8] R. P. Feynman, *Application of Quantum Mechanics to Liquid Helium*. Progress in Low Temperature Physics **1**, (1955).

[9] K. W. Schwarz, *Turbulence in superfluid helium: Steady homogeneous counterflow*. Phys. Rev. B, Vol. **18**, No. 1, (1978).

[10] M. S. Paoletti, M. E. Fisher, K. R. Sreenivasan, and D. P. Lathrop, *Velocity Statistics Distinguish Quantum Turbulence from Classical Turbulence*. Phys. Rev. Lett. **101**, 154501, (2008).

[11] R. J. Donnelly, *Quantized Vortices in Helium II*. Cambridge University Press, (1991).

[12] S. Babuin, E. Varga, L. Skrbek, *The Decay of Forced Turbulent Coflow of He II Past a Grid*. J. Low Temp. Phys. **175**:324–330, (2014).

[13] P. M. Walmsley, A. I. Golov, H. E. Hall, A.A. Levchenko, W.F. Vinen, Phys. Rev. Lett. **99**, 265302 (2007)

[14] D. V. Osborne, Proc. Phys. Soc. A **63**, 909 (1950).

[15] J. Maurer, P. Tabeling, Europhys. Lett. **43**, 29 (1998).

[16] S. Babuin, E. Varga, L. Skrbek, E. Lévêque, P.-E. Roche, *Effective viscosity in quantum turbulence: a steady-state approach*. Europhys. Lett. **106**, 24006 (2014).

[17] W.F. Vinen, *Mutual Friction in a Heat Current in Liquid Helium II. III. Theory of the Mutual Friction*. Proc. R. Soc. Lond. A **242**, (1957).

[18] E. Varga, S. Babuin, L. Skrbek, *Second-sound studies of coflow and counterflow of superfluid ^{4}He in channels*. Phys. Fluids **27**, 065101 (2015).

[19] V. P. Peshkov, *Second Sound in Helium II*. Soviet Physics JETP Vol. **11**, No. 3 (1960).

[20] R. J. Donnelly, and C. F. Barenghi, *The Observed Properties of Liquid Helium at the Saturated Vapor Pressure*. J. Phys. Chem. Ref. Data, Vol. **27**, No. 6, (1998).

[21] H. E. Hall, and W. F. Vinen, Proc. Roy. Soc. A **238** 204, 215, (1956).

[22] R. D. McCarty, *Thermophysical properties of Helium-4 from 2 to 1500 K with pressures to 1000 atmospheres*. National Bureau of Standards, (1972).

[23] V. Kotsubo, G. W. Swift, *Generation of Superfluid Vortex Turbulence by High-Amplitude Second Sound in ^{4}He*. J. Low Temp. Phys., Vol. **78**, Nos. 5/6, (1990).

[24] S. Babuin, E. Varga, W. F. Vinen, and L. Skrbek, *Quantum turbulence of bellows-driven ^{4}He superflow: Decay*. Phys. Rev. B. **92**, 184503 (2015).

[25] J. Gao, W. Guo, V. S. L'vov, A. Pomyalov, L. Skrbek, E. Varga, and W. F. Vinen, *Decay of Counterflow Turbulence in Superfluid ^{4}He*. JETP Letters, **103**, No. 10, pp. 648-652 (2016).

[26] E. Varga, M. J. Jackson, D. Schmoranzer, L. Skrbek, *The Use of Second Sound in Investigations of Quantum Turbulence in He II*. J. Low Temp. Phys., in print (2019).

[27] D. Schmoranzer, Doctoral Thesis:*Investigation of cryogenic helium flows using mechanical oscillators*. Charles University, Faculty of Mathematics and Physics, Prague, (2011).

[28] D. Schmoranzer, M. J. Jackson, Š. Midlik, M. Skyba, J. Bahyl, T. Skokánková, V. Tsepelin, and L. Skrbek, *Dynamical similarity and instabilities in high-Stokes-number oscillatory flows of superfluid helium*. Phys. Rev. B. **99**, 054511 (2019).

[29] M. J. Jackson, Doctoral Thesis:*A Study of Quantum Turbulence in Superfluid ^{3}He-B Using Vibrating Structures*. Lancaster University, (2011).

[30] S. Babuin, M. Stammeier, E. Varga, M. Rotter, L. Skrbek, *Quantum turbulence of bellows-driven ^{4}He superflow: Steady state*. Phys. Rev. B. **86**, 134515 (2012).

[31] E. Varga, Master Thesis: *Steady state and decay of quantum turbulence generated in channel flows and detected by second sound attenuation*. Charles University, Faculty of Mathematics and Physics, Prague, (2014).

A. Attachments

Here, we present a published study on oscillatory flows in superfluid helium which was mainly conducted in our laboratory to which the author of this thesis contributed by studying oscillatory flows around a vibrating micro-wire.

A.1 Attachment 1. Dynamical similarity and instabilities in high-Stokes-number oscillatory flows of superfluid helium [28]